Submitted to the Astrophysical Journal

Fragmentation of a Molecular Cloud Core versus Fragmentation of the Massive Protoplanetary Disk in the Main Accretion Phase

Tomoaki Matsumoto[1,2]

matsu@i.hosei.ac.jp

and

Tomoyuki Hanawa[3]

hanawa@cfs.chiba-u.ac.jp

ABSTRACT

The fragmentation of molecular cloud cores a factor of 1.1 denser than the critical Bonnor-Ebert sphere is examined though three-dimensional numerical simulations. A nested grid is employed to resolve fine structure down to 1 AU while following the entire structure of the molecular cloud core of radius 0.14 pc. A barotropic equation of state is assumed to take account of the change in temperature during collapse, allowing simulation of the formation of the first core. A total of 225 models are shown to survey the effects of initial rotation speed, rotation law, and amplitude of bar mode perturbation. The simulations show that the cloud fragments whenever the cloud rotates sufficiently slowly to allow collapse but fast enough to form a disk before first-core formation. The latter condition is equivalent to $\Omega_0 t_{\rm ff} \gtrsim 0.05$, where Ω_0 and $t_{\rm ff}$ denote the initial central angular velocity and the freefall time measured from the central density, respectively. Fragmentation is classified into six types: *disk-bar*, *ring-bar*, *satellite*, *bar*, *ring*, and *dumbbell* types according to the morphology of collapse and fragmentation. When the outward decrease in initial angular velocity is more steep, the

[1]Department of Humanity and Environment, Hosei University, Fujimi, Chiyoda-ku, Tokyo 102-8160, Japan

[2]Theoretical Astrophysics, National Astronomical Observatory, Mitaka, Tokyo 181-8588, Japan

[3]Center for Frontier Science, Chiba University, Yayoi-cho, Inage-ku, Chiba, 263-8522, Japan

cloud deforms from spherical at an early stage. The cloud deforms into a ring only when the bar mode ($m = 2$) perturbation is very minor. The ring fragments into two or three fragments via *ring-bar* type fragmentation and into at least three fragments via *ring* type fragmentation. When the bar mode is significant, the cloud fragments into two fragments via either *bar* or *dumbbell* type fragmentation. These fragments eventually merge due to their low angular momenta, after which several new fragments form around the merged fragment via *satellite* type fragmentation. This satellite type fragmentation may be responsible for observed wide range of binary separation.

Subject headings: binaries: general — hydrodynamics — ISM: clouds — methods: numerical — stars: formation

1. Introduction

It is widely accepted that binary and multiple stars form as a result of fragmentation in collapsing molecular cloud cores (e.g., Bodenheimer et al. 2000). In the last two decades, fragmentation of the molecular cloud core has been investigated through numerical simulations by many authors. Criteria for the fragmentation of isothermally collapsing clouds has been investigated by Miyama, Hayashi, & Narita (1984); Boss (1993); Boss & Myhill (1995); Tsuribe & Inutsuka (1999). Their criteria have converged as far as the isothermal phase is concerned; a cloud with $\alpha \lesssim 0.2 - 0.5$ collapses into fragments depending little on β, even when the initial density and velocity distributions differ. Here, α and β denote the ratio of thermal energy to gravitational energy and that of rotation energy to gravitational energy, respectively. Tsuribe & Inutsuka (1999) pointed out that the criteria for fragmentation corresponds to the formation of a flat disk with flatness greater than 4π. On the other hand, a cloud with $\alpha \gtrsim 0.2 - 0.5$ collapses self-similarly and shows no sign of fragmentation. Hanawa & Matsumoto (1999) and Matsumoto & Hanawa (1999) investigated deformation of the self-similarly collapsing cloud in search of the possibility that deformation of the central cloud to a bar might trigger fragmentation. The growth of the bar mode is slow compared to the timescale of the collapse, i.e., $\Delta \propto \rho_{\rm max}^{0.177}$, where Δ and $\rho_{\rm max}$ denote the amplitude of the bar mode and the maximum density of the cloud, respectively. The bar may indeed fragment, but only at a later stage.

As the collapse proceeds, the cloud core becomes optically thick and the efficiency of radiative cooling decreases. The temperature starts increasing when the central density exceeds the critical density of $\sim 10^{-13}\,{\rm g\,cm^{-3}}$. This increase in temperature results in the formation of a quasi-static core, i.e., the first core of Larson (1969). The first core grows

by accreting gas, and this accretion phase persists for long enough for the core to fragment. Thus, the dynamics of the cloud changes qualitatively at the critical density. Stability against fragmentation is also likely to change at this critical density. In fact, the first core has been shown by recent simulations to be very unstable taking account of the change in temperature (Burkert, Bate, & Bodenheimer 1997; Nelson 1998; Sigalotti 1998; Klapp & Sigalotti 1998; Boss et al. 2000). Their simulations, however, assume rather small α. When α is small, the cloud is Jeans unstable and fragments easily (Tsuribe & Inutsuka 1999). The fragmentation of the first core may be due to the small α assumed. It is still unanswered whether the first core fragments when the initial cloud has a moderately large α. Thus, we investigate the fragmentation of the cloud with focus on the cloud with large α of 0.765. The initial cloud is only 1.1 times more massive than the critical Bonnor-Ebert sphere (Ebert 1955; Bonnor 1956), which is an equilibrium state of the isothermal cloud.

The Bonnor-Ebert sphere provides a good fit to the density distribution of a dark globule. According to recent near-infrared observations (Alves, Lada, & Lada 2001), the model with $\xi = 6.9 \pm 0.2$ gives the best fit for B68, where ξ denotes the non-dimensional radius. Similarly, those with $\xi = 12.5 \pm 2.6$ and 7.0 ± 0.3 give a good fit for B335 (Harvey et al. 2001) and the Coalsak (Racca, Gómez, & Kenyon 2002), respectively. When $\xi > 6.45$, the Bonnor-Ebert sphere is unstable against collapse. Thus, our initial model can be applied to these globules.

The model can also be applied to cloud cores embedded with molecular clouds. The masses of such cores evaluated from $C^{18}O$ luminosity are similar to the virial masses (e.g., Onishi et al. 1996). This implies that the cores are gravitationally bound and nearly in equilibrium, and accordingly, the parameter α is only slightly less than unity.

Recent numerical studies have lacked any survey of model parameters. In this study, 225 models with different rotation speed, rotation law, and amplitude of bar mode perturbation are considered. The simulations show many types of fragmentation, some of which are new. The main features of each type and the territory of each type in the parameter space are discussed.

In this paper, the collapse and fragmentation of molecular cloud cores is investigated using a nested grid. The nested grid has high spatial resolution near the center of the computation domain and allows fragmentation to be followed without violating the Jeans condition (Truelove et al. 1997). In §2, the models of cloud cores are introduced. In §3, the methods of numerical simulations are presented. In §4, the results are shown and the fragmentation is classified. In §5, the origins of different types of fragmentation are discussed, the simulations are compared with earlier numerical works, the implications on binary formation are related. The paper is concluded in §6.

2. Models

As a model for molecular cloud cores, we consider Bonnor-Ebert spheres, which belong to a sequence of equilibrium-state isothermal spherical clouds confined by external pressure (Ebert 1955; Bonnor 1956). Given the external pressure ($P_{\rm ex}$) and the sound speed (c_s), the Bonnor-Ebert sphere is stable against collapse only when the central density is lower than the critical value, $14.0\,P_{\rm ex}/c_s^2$. The critical Bonnor-Ebert sphere is used as a template for the model clouds examined in this study. In the models, the initial density distribution is given by

$$\rho(r) = \rho_c \varrho_{\rm BE}(r/a) \tag{1}$$

and

$$a = c_s \left(\frac{f}{4\pi G \rho_c} \right)^{1/2} , \tag{2}$$

where r, f, ρ_c and G denote the radius, density enhancement factor, the initial central density, and the gravitational constant, respectively. The function $\varrho_{\rm BE}$ denotes the density distribution of the critical Bonnor-Ebert sphere, and can be approximated as

$$\varrho_{\rm BE}(\xi) = 1 - \frac{\xi^2}{6} + \frac{\xi^4}{45} + \mathcal{O}(\xi^6) \, . \tag{3}$$

The critical Bonnor-Ebert sphere has radius of $\xi = 6.45$. A density enhancement factor of $f = 1.1$ is assumed in typical models because observed molecular clouds are nearly in the virial equilibrium. This slight density enhancement collapses rotating clouds when the initial cloud rotates slowly.

The initial central density is set at $\rho_c = 1 \times 10^{-19}\,{\rm g\,cm^{-3}}$, which corresponds to a number density of $n_c = 2.6 \times 10^4\,{\rm cm^{-3}}$ for the assumed mean molecular weight of 2.3. An initial temperature of $T = 10\,{\rm K}$ is assumed, and hence $c_s = 0.19\,{\rm km\,}s^{-1}$. The radius and mass of the cloud are thus $R_c = 0.144$ pc and $M = 3.24\,M_\odot$ for $f = 1.1$.

The initial velocity includes only the φ-component, and the angular velocity depends on R and φ in cylindrical coordinates (R, φ, z). The angular velocity Ω is expressed as

$$\Omega(R,\varphi) = \left[\Omega_0 + \Omega_2 \cos(2\varphi) + \Omega_3 \left(\frac{R}{a} \right) \cos(3\varphi) \right] \left[1 + 2C \left(\frac{R}{a} \right)^2 \right]^{-1/2} , \tag{4}$$

where Ω_0 denotes the amplitude of the global rotation, and Ω_2 and Ω_3 denote the amplitudes of the velocity perturbation of $m = 2$ and 3. The parameter C specifies the dependence of Ω on R. When $C = 0$, the angular velocity is independent of R and rotation is "rigid". When C is larger, the angular velocity decreases more rapidly with increasing in R. As shown later,

fragmentation of the cloud core depends strongly on the parameter C. A small amplitude for the perturbation of $m = 3$ is set, such as $\Omega_3 t_{\rm ff} = 1 \times 10^{-3}$, in all the models, where $t_{\rm ff}$ denotes the initial freefall timescale at the center and is defined as $(3\pi/32G\rho_c)^{1/2}$. This $m = 3$ mode breaks the point symmetry with respect to $R = 0$, and accordingly the fragments are slightly asymmetric in this simulation. The model parameters Ω_0, Ω_2, and C are varied to investigate the effects of rotation speed, amplitude of the bar mode, and the rotation law on fragmentation of the cloud cores.

To compare our initial models with those of earlier simulations, the ratios $\alpha = E_{\rm th}/|E_{\rm grav}|$ and $\beta = E_{\rm rot}/|E_{\rm grav}|$ are computed, where $E_{\rm th}$, $E_{\rm rot}$, and $E_{\rm grav}$ are thermal energy, rotation energy, and gravitational energy, respectively (e.g., Tohline 1981; Miyama et al. 1984). In our model, the initial cloud has $\alpha = 0.765\,(1.1/f)$. The parameter β is independent of f, and when $\Omega_3 = 0$, β is described by

$$\beta = \beta_C t_{\rm ff}^2 \left(\Omega_0^2 + \frac{1}{2}\Omega_2^2 \right) \ , \tag{5}$$

where the coefficient β_C is a function of C as shown in Figure 1. When a cloud rotates rigidly ($C = 0$), it has $\beta_C = 0.892$. When $C \sim 1$, β_C decreases approximately in proportion to $C^{-1/2}$. The decrease in β_C is due to slow rotation in the outer part of the cloud.

When α and β are small, the cloud is unstable against fragmentation. When the cloud has uniform density and rotates rigidly, the criterion for fragmentation is $\alpha \lesssim 0.5$ (e.g., Tsuribe & Inutsuka 1999). When the cloud is centrally peaked and the axis ratio is 1.5, the criterion is $\alpha \lesssim 0.45$ for low β (Boss 1993). When the cloud is more oblate, i.e., the axis ratio is 2.0, the criterion is $\alpha \lesssim 0.33$ for low β. This suggests that a cloud of $\alpha \gtrsim 0.5$ is stable against fragmentation. In this study, the possibility of fragmentation of a cloud with $\alpha > 0.7$ is examined.

The dynamical evolution of a cloud is followed taking account of the self-gravity and gas pressure. The magnetic field is neglected for simplicity. The gas temperature is assumed to be 10 K below the critical density $\rho_{\rm cr} = 2 \times 10^{-13}\,{\rm g\,cm^{-3}}$ ($n_{\rm cr} = 5.24 \times 10^{10}\,{\rm cm^{-3}}$), and to increase adiabatically in proportion to $\rho^{2/5}$ above it. In other words, a barotropic equation of state is assumed, as expressed by

$$P = \begin{cases} c_s^2 \rho & \text{for } \rho < \rho_{\rm cr} \\ c_s^2 \rho_{\rm cr} (\rho/\rho_{\rm cr})^{7/5} & \text{for } \rho \geq \rho_{\rm cr} \end{cases} \ . \tag{6}$$

This change in temperature reproduces the formation of the adiabatic core, which corresponds to the first core of Larson (1969). The value of the critical density $\rho_{\rm cr}$ is taken from the numerical results of Masunaga, Miyama, & Inutsuka (1998), who studied the spherical collapse of molecular cloud cores with radiative hydrodynamics.

3. Numerical Methods

In the simulations, the hydrodynamical equation and Poisson equation are solved by a finite difference method with second-order accuracy in time and space. A nested grid is employed to solve the central region with higher spatial resolution. The hydrodynamic code for the nested grid was developed by extending the simulation code of Matsumoto & Hanawa (1999). The nested grid consists of concentric hierarchical rectangular grids (Yorke, Bodenheimer, & Laughlin 1993), and the cell width of each grid decreases successively by a factor of two. In the following, the coarsest grid is labeled level $l = 1$. The l-th level grid has 2^{l-1} times higher spatial resolution than the coarsest grid. All the fluxes are conserved at the interface between the coarse and fine grids as in the standard adaptive mesh refinement (AMR; Chiang, van Leer, & Powell 1992). Thus, the total mass is conserved in our computations. The numerical fluxes are obtained by the method of Roe (1981) with modification to solve the isothermal and polytrope gas. A MUSCL approach and predictor-corrector method are adopted for time integration (e.g., Hirsch 1990). The Poisson equation is solved by a multigrid iteration on a nested gird (Matsumoto & Hanawa 2003). This code solves self-gravity consistently over all grids with different levels such that "the gravitational field line" is continuous at interfaces between coarse and fine grids. This consistency ensures that the obtained gravitational potential is accurate at least up to the quadrapole moment of a binary. Thus, the gravitational torque induced by a binary is accurately taken into account in our simulation.

Mirror symmetry with respect to the $z = 0$ plane is employed to reduce computation cost. A fixed boundary condition is set for the surface of $r = R_c$, representing a constant external pressure that confines the cloud during evolution. Gas is considered only in $r \leq R_c$ when solving the Poisson equation.

In this paper, each grid has $256 \times 256 \times 32$ cubic cells in high-resolution models, and $128 \times 128 \times 16$ cubic cells in low-resolution models in (x, y, z). The model parameters of the high-resolution models are shown in Table 1. The other models shown in this paper are the low-resolution models. The nested grid consists of grids of 5 levels at the initial stage. A new finer grid is introduced to maintain the Jeans condition of $\lambda_{\rm J}/4 > h$ with ample margin (Truelove et al. 1997), where $\lambda_{\rm J}$ and h are the Jeans length and cell width, respectively. Whenever an eighth of the minimum Jeans length ($\lambda_{\rm J,min}$) became smaller than the cell width in the finest grid, a new finer grid was added to the nested grid. This means that a finer grid was added with ample margin of factor 2. Typical models have 14 grid levels at the last stage. The Jeans condition was only violated in these simulations when a high density fragment escaped from the region covered by the finest grid, and the computation was terminated in the stage that this occurred. In the model shown in §4.1.1, evolution was

successfully computed up to the stage in which the mass of an adiabatic core (total mass in the region of $\rho \geq \rho_{\rm cr}$) reached 0.07 $M_\odot$.

4. Results

4.1. Rigidly Rotating Cloud

In this subsection, a total of 27 models of a rigidly rotating cloud ($C = 0$) in the region $0.03 \leq \Omega_0 t_{\rm ff} \leq 0.3$ and $0 \leq \Omega_2 t_{\rm ff} \leq 0.3$ are presented to study the dependence on Ω_0 and Ω_2.

Figure 2 summarizes the last stages of the 27 models. Each panel denotes the density distribution in the $z = 0$ plane. The panels are arranged such that Ω_0 increases from left to right and Ω_2 increases from bottom to top. The evolutions of the clouds are classified into five types in the parameter space of the initial rotation ($\Omega_0 t_{\rm ff}$) and the initial amplitude of bar mode ($\Omega_2 t_{\rm ff}$). When $\Omega_0 t_{\rm ff} \leq 0.03$ (left column), the cloud collapses to form a single disk (*disk* type collapse). When $\Omega_0 t_{\rm ff} = 0.3$ (right column), the cloud never collapses, and instead oscillates. When $0.05 \leq \Omega_0 t_{\rm ff} \leq 0.2$ (middle three columns), the cloud collapses into several fragments. The last type is further subdivided into three types: *disk-bar*, *ring-bar*, and *satellite* types. In the following, each type is discussed by showing a typical model.

4.1.1. Disk type collapse

In *disk* type collapse, the cloud collapses almost spherically in the isothermal collapse phase and forms a rotating disk after the central density exceeds the critical density $\rho_{\rm cr}$. The disk grows by accretion and exhibits no sign of fragmentation. The model of ($\Omega t_{\rm ff}, \Omega_2 t_{\rm ff}$, C) = (0.03, 0.03, 0.0) is shown in Figure 3 as typical model of *disk* type collapse.

Figure 3*a* shows the initial stage, showing only the finest three grids ($3 \leq l \leq 5$), i.e., only 1/64 of the full computation volume. The initial cloud has a spherical density distribution, and the cloud collapses almost spherically during the isothermal collapse phase ($\rho < \rho_{\rm cr}$) as a result of the very slow rotation. When $\rho \simeq \rho_{\rm cr}$, the central cloud becomes slightly flattened by the rotation and deforms non-axisymmetrically due to perturbation of the bar mode (Figure 3*b*).

The deformation is evaluated by measuring the moment of inertia,

$$I_{ij} = \int_{\rho \geq 0.1\rho_{\rm max}} (r_i - r_{g,i})(r_j - r_{g,j})\rho(\boldsymbol{r}) d\boldsymbol{r} \ , \tag{7}$$

and the total mass,

$$M = \int_{\rho \geq 0.1\rho_{\rm max}} \rho(\boldsymbol{r}) d\boldsymbol{r} \ , \tag{8}$$

for the gas of $\rho \geq 0.1\rho_{\rm max}$. The subscripts i and j are coordinate labels, i.e., $x = r_1$, $y = r_2$, and $z = r_3$. The barycenter is defined as

$$r_{g,i} = \frac{1}{M} \int_{\rho \geq 0.1\rho_{\rm max}} \rho r_i d\boldsymbol{r} \ . \tag{9}$$

The long axis (a_l), short axis (a_s), and length along the z-axis (a_z) are defined by

$$\left(\begin{array}{c} a_l^2 \\ a_s^2 \\ a_z^2 \end{array} \right) = \frac{1}{2M} \left\{ \begin{array}{l} I_{11} + I_{22} + [(I_{11} - I_{22})^2 + 4I_{12}^2]^{1/2} \\ I_{11} + I_{22} - [(I_{11} - I_{22})^2 + 4I_{12}^2]^{1/2} \\ 2I_{33} \end{array} \right\} \ . \tag{10}$$

Figure 4 shows eccentricity ($a_l/a_s - 1$) and flatness [$(a_l a_s)^{1/2}/a_z - 1$] as functions of the maximum number density $n_{\rm max}$. The eccentricity oscillates with significant amplitude in the range $10^4\,{\rm cm}^{-3} \leq n_{\rm max} \lesssim 10^6\,{\rm cm}^{-3}$, and increases roughly in proportion to $n_{\rm max}^{1/6}$ in the range $10^6\,{\rm cm}^{-3} \lesssim n_{\rm max} \lesssim 10^{10}\,{\rm cm}^{-3}$ due to bar mode instability (Hanawa & Matsumoto 1999; Matsumoto & Hanawa 1999). At the end of the isothermal collapse phase, the long axis is 12% longer than the short axis (eccentricity is 0.122). The flatness, $a_l/a_z - 1$, increases due to spin-up in the central cloud. In the range $10^8\,{\rm cm}^{-3} \lesssim n_{\rm max} \lesssim 10^{11}\,{\rm cm}^{-3}$, the flatness increases rapidly in proportion to $n_{\rm max}^{0.7}$. At the end of the isothermal collapse phase, the flatness is 0.412 and the long axis is 50% longer than thickness in the z-direction.

Figure 4 also shows the central angular velocity in unit freefall time $\Omega t_{\rm ff}$. The angular velocity and the freefall time are measured as $\Omega = J_{{\rm spin},z}/[M(a_l^2 + a_s^2)]$ and $t_{\rm ff} = (3\pi/32G\rho_{\rm max})^{1/2}$, where $J_{{\rm spin},z}$ denotes the z-component of the total spin angular momentum $\boldsymbol{J}_{\rm spin}$, which is defined as

$$\boldsymbol{J}_{\rm spin} = \int_{\rho \geq 0.1\rho_{\rm max}} (\boldsymbol{r} - \boldsymbol{r}_g) \times (\boldsymbol{v} - \boldsymbol{v}_g) \rho d\boldsymbol{r} \ , \tag{11}$$

where

$$\boldsymbol{v}_g = \frac{1}{M} \int_{\rho \geq 0.1\rho_{\rm max}} \boldsymbol{v} \rho d\boldsymbol{r} \ . \tag{12}$$

This angular velocity represents the average angular velocity in the region of $\rho \geq 0.1\rho_{\rm max}$, and is denoted $\Omega_{0.1}$. Another average angular velocity $\Omega_{0.5}$, defined in the region of $\rho \geq 0.5\rho_{\rm max}$, is also introduced in order to measure the value near the center. At the initial stage, $\Omega_{0.1}$ and $\Omega_{0.5}$ have the same value because the initial cloud rotates rigidly. In the early isothermal collapse phase, the central part rotates faster ($\Omega_{0.5} > \Omega_{0.1}$). For $n_{\rm max} \lesssim 10^8\,{\rm cm}^{-3}$, the cloud

spins up according to $\Omega_{0.5} t_{\rm ff} \propto n_{\rm max}^{1/6}$, in other words, $\Omega_{0.5} \propto n_{\rm max}^{2/3}$. This spin-up rate coincides with that expected for spherical collapse (Hanawa & Nakayama 1997). The cloud collapses almost spherically in the isothermal collapse phase, and significant deformation only occurs near the end of the isothermal collapse phase. The maximum value of $\Omega_{0.5} t_{\rm ff}$ is 0.0973.

When the central density exceeds $\rho_{\rm cr}$, the infall decelerates near the center and an adiabatic core, the first core, forms. The first core of Larson (1969) is quasi-static and spherical, whereas this adiabatic core is rotating and disk-like. The adiabatic core formation ends the isothermal collapse phase. Infall still continues in the region far from the center, and the adiabatic core accretes gas from the envelope. Thus, the period after adiabatic core formation is called the accretion phase. Figure 3*c* shows the adiabatic core at the stage of $t - t_{\rm cr} = 216\,{\rm yr}$, where $t_{\rm cr}$ denotes the time at which $\rho_{\rm max}$ exceeds $\rho_{\rm cr}$. The adiabatic core consists of a flattened central kernel with an envelope of adiabatic gas. The kernel has a radius of 2 AU and a thickness of 1.5 AU. The mass of the kernel is $M_{13} = 7.4 \times 10^{-3}\,M_\odot$, where M_N denotes the mass measured for $n \geq 10^N\,{\rm cm}^{-3}$.

Figure 3*d* shows the adiabatic core at the stage of $t - t_{\rm cr} = 775\,{\rm yr}$, after it has begun to accrete gas from the isothermal infalling envelope. The adiabatic core at this stage consists of a flattened central kernel with an extended disk and spiral arms. One of the dense spiral arms evolves into a dense clump, as can be seen to the upper left of the central kernel in Figure 3*d*. The dense clump falls into the central kernel and merges into it. Figure 3*e* shows the adiabatic core after the merge of the dense clump ($t - t_{\rm cr} = 838\,{\rm yr}$). The radius of the adiabatic disk increases to 15 AU by this stage. During the period $1.0 \times 10^3\,{\rm yr} \lesssim t - t_{\rm cr} \lesssim 1.1 \times 10^3\,{\rm yr}$, this formation and merging of a clump occurs again. During the formation of the clump, the disk shrinks to 10 AU. However after merging, the radius of the adiabatic disk increases to 20 AU. Figure 3*f* shows the last stage of the simulation ($t - t_{\rm cr} = 1.5 \times 10^3\,{\rm yr}$). The radius of the adiabatic disk has increased to 20 AU, although the radius of the central kernel remains. The masses of the adiabatic core and the kernel are $6.9 \times 10^{-2}\,M_\odot$ and $4.2 \times 10^{-2}\,M_\odot$ at this stage.

Figure 5 shows the sizes of the adiabatic core (a_l, a_s, a_z) as a function of time. These sizes were evaluated in the same manner as in Figure 4 except that the volume of integration was bounded by $\rho \geq \rho_{\rm cr}$ in equations (7), (8), and (9). Note that the sizes evaluated from the moment of inertia correspond to the scale length of the cloud and are several times smaller than the cloud radius. For example, a_l, a_s, and a_z are by a factor of $5^{-1/2} = 0.447$ smaller than the radius a for a spherical cloud having uniform density. The vertical scale height remains approximately $a_z = 1 - 1.5$ AU, whereas a_l and a_s increase while oscillating significantly. The average growth rate is roughly $da_l/dt = da_s/dt \sim 3 \times 10^{-3}\,{\rm AU\,yr}^{-1}$. These sizes undergo two types of oscillation beyond the steady growth. First, large peaks

appear near $t - t_{\rm cr} = 800$ yr and 1100 yr. This synchronous oscillation corresponds to the formation and merging of the dense clumps in the adiabatic disk. The disk has a small radius during formation, and then expands greatly after merging. Second, a_l and a_s exhibit an anti-correlation with small amplitude on a short timescale. This anti-correlation is due to intermittent excitation of spiral arms, which transfer angular momentum from the adiabatic disk to the outer infalling envelope. These recurrently excited spiral arms are also seen in Saigo, Hanawa & Matsumoto (2003), in which growth of the first core was investigated.

Figure 5 also shows the mass of the adiabatic core as a function of time. The mass increases monotonically due to accretion. The average accretion rate is approximately $5 \times 10^{-5}\,M_\odot$ yr^{-1}.

The formation of the dense clump and excitation of the spiral arms are examined here based on the linear stability of Toomre (1964). A thin disk is unstable when the following two conditions are satisfied simultaneously. First, the Toomre Q-value defined as

$$Q = \frac{c\kappa}{\pi G\Sigma} \tag{13}$$

must be smaller than unity in the region of interest, where c, κ and Σ are the sound speed, the epicyclic frequency, and the surface density, respectively. Second, the unstable region should be larger than the critical Jeans length,

$$\lambda_c = \frac{2c^2}{G\Sigma}\left[1 + \left(1 - Q^2\right)^{1/2}\right]^{-1} \ . \tag{14}$$

These criteria are applied to our simulation by evaluating

$$\Sigma(x,y) = \int_{\rho>\rho_{\rm cr}} \rho(x,y,z)dz \ , \tag{15}$$

$$c(x,y) = \frac{1}{\Sigma(x,y)}\int_{\rho>\rho_{\rm cr}} \left[\frac{dP}{d\rho}(x,y,z)\right]^{1/2} \rho(x,y,z)dz \ , \tag{16}$$

$$\kappa(x,y) = \left(4\bar{\Omega}^2 + R\frac{d\bar{\Omega}^2}{dR}\right)^{1/2} \ , \tag{17}$$

and

$$\bar{\Omega}(x,y) = \frac{1}{\Sigma(x,y)}\int_{\rho>\rho_{\rm cr}} \frac{v_\varphi(x,y,z)}{R}\rho(x,y,z)dz \ . \tag{18}$$

Figure 6*a* shows the distribution of the critical Jeans length $\lambda_c(x,y)$ for the stage shown in Figure 3*d*. The surface density Σ takes a positive value within the domain indicated by the closed thick curve, i.e., edge of the adiabatic disk. The Toomre Q-value is less than unity in the gray regions, and larger than unity in the white regions. It is less than unity only in

the central kernel, dense clump and spiral arms. The rest of the disk has $Q > 1$ and the disk is globally stable against the ring mode. The critical Jeans lengths are less than 1 AU in both the central kernel and the dense clump, which is roughly 1 AU in size. Thus, both are self-gravitationally bounded. Figure 6*b* shows the same results for the last stage. The Q-value is less than unity only in the kernel and the spiral arms. The spiral arms have width of 2.5 AU in the central region of $r \lesssim 5\,\mathrm{AU}$, where the critical Jeans length is less than 2.5 AU. In the outer region of $r \gtrsim 10\,\mathrm{AU}$, the critical Jeans length is $5 - 7.5$ AU and the spiral arms have width of 7.5 AU. Thus, the inner and outer spiral arms are self-gravitating and can be supposed to form by gravitational instability.

4.1.2. Disk-bar type fragmentation

In the models of *disk-bar* type fragmentation, $(\Omega_0 t_{\rm ff},\, \Omega_2 t_{\rm ff},\, C) = (0.05,\, 0.0,\, 0.0)$ and $(0.05,\, 0.01,\, 0.0)$, the cloud collapse is almost axisymmetric in the isothermal collapse phase resulting in the formation of a disk in the beginning of the accretion phase. The disk deforms to a bar-shape in the early accretion phase. Thereafter, the bar fragments into two fragments. This fragmentation is called *disk-bar* type. The model of $(\Omega_0 t_{\rm ff},\, \Omega_2 t_{\rm ff},\, C) = (0.05,\, 0.0,\, 0.0)$ is shown in Figure 7 as a typical model of *disk-bar* type fragmentation.

In the initial stage, the cloud undergoes uniform rotation with a small $m = 3$ perturbation (no $m = 2$ perturbation). The cloud collapse is almost axisymmetric in the isothermal collapse phase. Figure 7*b* shows the cloud at the end of the isothermal collapse phase. The central cloud is slightly flattened due to the rotation.

Figure 8 shows the evolution of flatness $[(a_l a_s)^{1/2}/a_z - 1]$, eccentricity $(a_l/a_s - 1)$, and angular velocity $(\Omega t_{\rm ff})$ for the central cloud in the isothermal collapse phase. The flatness increases rapidly in proportion to $\rho_{\rm max}^{0.3}$. At the end of the isothermal collapse phase, a disk forms with flatness of 0.439. The eccentricity remains small because the initial cloud has only a small $m = 3$ perturbation, with no bar mode perturbation. The angular velocity $(\Omega t_{\rm ff})$ is relatively large at the beginning, and increases according to $\Omega_{0.5} \propto n_{\rm max}^{1/6}$ up to $\Omega_{0.5} t_{\rm ff} = 0.452$ in the isothermal collapse phase. The growth rate of $\Omega_{0.5} t_{\rm ff}$ is similar to that shown in Figure 4 for the *disk* type collapse model.

Figure 7*b* shows the adiabatic core at the stage of $t - t_{\rm cr} = 301$ yr. The adiabatic core at this time consists of a flat disk with an envelope. The adiabatic disk deforms to a bar-shape at $t - t_{\rm cr} = 439$ yr, as shown in Figure 7*c*, due to self-gravitational instability. The seed of the bar mode is discretization error in this model. Figure 9 shows the distribution of critical Jeans length for the stage shown in Figure 7*b*. The elliptical disk of 12 AU $\times$

11 AU has a critical Jeans length of $2 - 4$ AU, except in the region of the central holes, $r \lesssim 2\,\mathrm{AU}$. The disk thus suffers from gravitational instability and deforms to a bar. The bar fragments into two fragments at $t - t_{\rm cr} \simeq 500$ yr, with masses of $M_{13} = 1.0 \times 10^{-2}\,M_\odot$ and $1.1 \times 10^{-2}\,M_\odot$, and $M_{14} = 4.8 \times 10^{-3}\,M_\odot$ and $3.0 \times 10^{-3}\,M_\odot$. The fragments rotate around each other and accrete gas from the envelope. Figure 7*d* shows the fragments at the stage of $t - t_{\rm cr} = 1622$ yr. Similar to the adiabatic core shown in Figure 3*f*, each fragment has a central kernel and spiral arms embedded in an extended disk. At this stage, the two fragments have mass of $M_{13} = 3.0 \times 10^{-2}\,M_\odot$ and $2.4 \times 10^{-2}\,M_\odot$, and $M_{14} = 1.8 \times 10^{-2}\,M_\odot$ and $1.9 \times 10^{-2}\,M_\odot$.

Figure 10*a* shows the loci of fragments for the period between the stages of fragmentation and Figure 7*d* (468 yr $\leq t - t_{\rm cr} \leq$ 1622 yr). In this period of 1.1×10^3 yr, both fragments rotate approximately three and half times, increasing in separation. The time variation of the separation is shown quantitatively in Figure 11. The separation of the fragments increases from 11.6 AU with significant oscillation due to the eccentricity of the orbits. The fragments attain a maximum separation of 30.6 AU at $t - t_{\rm cr} = 1622$ yr (at the stage of Figure 7*d*). As the separation increases, the specific orbital angular momentum also increases by a factor of 4.9.

Figure 10*b* shows the situation after the maximum separation. After the stage of Figure 7*d*, the separation begins to decrease, to ~ 7 AU in only ~ 300 yr, as shown in Figure 11. The specific orbital angular momentum also decreases by a factor of 0.28. In this period, the fragments rotate only half a rotation. After the rapid decrease in the separation, the fragments rotate approximately 1.5 revolutions with a nearly constant separation of ~ 7 AU until the last stage. Figures 7*e* and 7*f* show the last stage of the simulation at different magnifications. At this stage, the fragments are separated by 6.7 AU, and surrounded by a circumbinary disk with tightly winding spiral arms that transfer the orbital angular momentum of the fragments to the circumbinary disk. The decrease in separation is due to the formation of the circumbinary disk. At the last stage, the two fragments have the same mass of $M_{14} = 2.4 \times 10^{-2}\,M_\odot$.

4.1.3. Ring-bar type fragmentation

In the models showing *ring-bar* type fragmentation, $(\Omega_0 t_{\rm ff},\, \Omega_2 t_{\rm ff},\, C) = (0.1,\, 0.0,\, 0.0)$, $(0.1,\, 0.01,\, 0.0)$, and $(0.2,\, 0.0,\, 0.0)$, cloud collapse is almost axisymmetric and a flat disk forms in the isothermal collapse phase. The disk deforms to a ring-shape temporarily, and then to a bar-shape in the early accretion phase. Thereafter, the bar fragments into two or three fragments. This fragmentation is called *ring-bar* type fragmentation. The model

of ($\Omega_0 t_{\rm ff}$, $\Omega_2 t_{\rm ff}$, C) = (0.1, 0.0, 0.0) is shown in Figure 12 as a typical example of *ring-bar* type fragmentation. This type of fragmentation is similar to *disk-bar* except for the transient formation of a ring and the number of fragments.

The initial stage is the same as for the previous model shown in §4.1.2 except for the initial uniform rotation speed. The cloud collapse is almost axisymmetric in the isothermal collapse phase. Figure 12*a* shows the cloud at the end of the isothermal collapse phase. The central cloud deforms to a disk-shape due to the rotation.

Figure 13 shows the evolution of flatness $[(a_l a_s)^{1/2}/a_z - 1]$, eccentricity $(a_l/a_s - 1)$, and angular velocity ($\Omega t_{\rm ff}$) for the central cloud in the isothermal collapse phase. These evolutions are similar to those for the *disk-bar* model. The flatness increases rapidly in proportion to $\rho_{\rm max}^{0.4}$. At the end of the isothermal collapse phase, a thin disk has formed, with flatness of 1.96. The eccentricity remains small because the initial cloud has only a small $m = 3$ perturbation and no bar mode perturbation. The angular velocity ($\Omega t_{\rm ff}$) is relatively large from the beginning, and increases according to $\Omega_{0.5} t_{\rm ff} \propto n_{\rm max}^{1/6}$ to a maximum of $\Omega_{0.5} t_{\rm ff} = 0.381$ at $n_{\rm max} = 5.46 \times 10^9\,{\rm cm}^{-3}$. When the central cloud is disk-like, $\Omega t_{\rm ff}$ becomes saturated.

Figure 12*b* shows the adiabatic core at $t - t_{\rm cr} = 563$ yr. The central adiabatic core is ring-like and surrounded by a flat isothermal envelope. The ring structure forms due to self-gravitational instability. Figure 14 shows the distribution of critical Jeans length for the stage shown in Figure 12*b*. The distribution is similar to that for the *disk-bar* model except that the adiabatic elliptical disk is larger roughly by a factor of two while the critical Jeans length is almost the same. The disk thus suffers from ring instability more strongly than in the *disk-bar* model.

The ring-shaped adiabatic core deforms to a rotating bar as shown in Figure 12*c*. The bar is twice as long as that in the *disk-bar* model, and the bar fragments into three fragments. Figure 12*d* shows the fragments at $t - t_{\rm cr} = 915$ yr. The central fragment is the most massive ($M_{13} = 2.0 \times 10^{-2}\,M_\odot$). The other fragments have masses of $M_{13} = 4.8 \times 10^{-3}\,M_\odot$ and $5.4 \times 10^{-3}\,M_\odot$.

Figure 15 shows the loci of the three fragments. The red and blue fragments rotate at a distance of roughly 15 AU, while the green fragment rotates around the red-blue close binary at distance of roughly 40 AU (see also Figure 12*e*). The three fragments form a hierarchical triple system.

Figure 12*f* shows the last stage of the simulation. The three fragments have similar masses of $M_{13} = 1.9 \times 10^{-2} M_\odot$ (red), $M_{13} = 1.7 \times 10^{-2} M_\odot$ (blue), and $M_{13} = 1.8 \times 10^{-2} M_\odot$ (green). The separation between the red and blue fragments is 14 AU, and that between the their barycenters and the green fragment is 41.6 AU at the last stage.

The calculation was terminated at this stage because the green fragment escaped from the region covered by the fine grid ($l = 13$) to that covered by the coarser grid ($l = 12$).

4.1.4. Satellite type fragmentation

In the models with $0.05 \leq \Omega_0 t_{\rm ff} \leq 0.2$ and with large $\Omega_2 t_{\rm ff}$, the cloud collapses to form a dense adiabatic core surrounded by an adiabatic disk. The disk suffers from self-gravitational instability and fragments into dense fragments orbiting around the central adiabatic core. The orbiting fragment is called a satellite fragment, and this fragmentation *satellite* type fragmentation. No appreciable difference between *satellite* type and *disk* type is seen up to disk formation. Spiral arms are excited in the adiabatic disk and local dense condensations form. The masses of these condensations exceed the Jeans mass, and evolve into satellite fragments confined by self-gravity. The satellite fragments orbit around the central core and exhibit close encounter, and sometimes merge during the accretion phase. In following, the model of ($\Omega_0 t_{\rm ff}$, $\Omega_2 t_{\rm ff}$, C) = (0.1, 0.05, 0.0) is shown as a typical example.

For the model of ($\Omega_0 t_{\rm ff}$, $\Omega_2 t_{\rm ff}$, C) = (0.1, 0.05, 0.0), the initial stage is the same as that of the previous model (*ring-bar* type) except for the amplitude of the bar mode. Figure 16*a* shows the cloud at the end of the isothermal collapse phase. The dense gas is flattened due to the rotation, and the cross section in the $y = 0$ plane resembles that of the previous model because of the same initial rotation (see Figure 12*a*). The central cloud is more elongated than in the previous model due to the large initial amplitude of the bar mode.

Figure 17*a* shows the distribution of critical Jeans length at the stage of adiabatic bar formation. Only a limited region along the axis is unstable against ring instability in the bar, while the adiabatic core is elongated into a bar.

Figure 16*b* shows the elongated adiabatic core. The central kernel (dense region in the adiabatic core) rotates differentially and excites spiral arms in the surrounding disk. The elongation of the central kernel precedes excitation of the ring instability as shown by Saigo et al. (2003). In their simulation, a cloud without the bar mode forms a ring-shaped core, while a cloud with the bar mode forms an elongated core with spiral arms. The amplitude of the bar mode separates the *satellite* type fragmentation from *disk-bar* and *ring-bar* types.

The spiral arms sweep up the disk and are wound up. These winding spiral arms then evolve into satellite fragments, which are confined by self-gravity, as shown in Figure 16*c*. Figure 17*b* shows the distribution of critical Jeans length at the stage of satellite fragment formation. The adiabatic disk is globally stable against the ring mode, yet is locally unstable in small regions around (x, y) $\simeq$ ($\pm$20 AU, $\mp$7 AU). A satellite fragment forms in each of

the local unstable regions.

Figure 18*a* shows the loci of the central fragment and the satellite fragments. The green locus denotes the central fragment, while the blue and red loci indicate the satellite fragments. The blue satellite fragment merges into the central fragment (green) after half a rotation, and the blue and red fragments form a binary system as shown in Figure 16*d*. The binary excites spiral arms and a new satellite fragment forms 519 yr after the merger. Figure 18*b* shows the loci after formation of the new satellite fragment. The purple locus denotes the new satellite fragment. The smallest fragment in Figure 16*e* is the new satellite fragment, which later falls into the green fragment resulting in a binary system again. Figure 16*f* shows the last stage of the simulation. At this stage, the masses of the fragments are $M_{13} = 2.0 \times 10^{-2} M_\odot$ (red) and $3.0 \times 10^{-2} M_\odot$ (green), and the separation between fragments is 26.9 AU.

4.2. Dependence on the Rotation Law

In this subsection, the dependence of the collapse and fragmentation on the rotation law specified by the parameter C is investigated. The azimuthally averaged angular velocity is independent of R (uniform) at $C = 0$, and decreases with increasing R as C gets larger.

Figure 19 shows the models of $\Omega_0 t_{\rm ff} = 0.2$ for the central 230 AU $\times$ 230 AU square at the stage of $\rho_c \simeq \rho_{\rm cr}$. Based on the morphology, these models can be classified into three types, i.e., *ring*, *bar*, and *dumbbell* types. Ring-shaped structures are seen in models with large C, while bar-shaped structures occur in models with large $\Omega_2 t_{\rm ff}$. When both C and $\Omega_2 t_{\rm ff}$ are large, the density has two peaks, and forms the *dumbbell* type. Both the dumbbell and ring forms in the model of $C \gtrsim 0.16$. Fragmentation, particularly the number of fragments, depends critically on the morphology.

The cloud with $\Omega_0 t_{\rm ff} \lesssim 0.03$ collapses to form an adiabatic disk and exhibits no sign of fragmentation (*disk* type collapse). On the other hand, a cloud with $\Omega_0 t_{\rm ff} \gtrsim 0.05$ fragments by any of the *disk-bar*, *ring-bar*, *satellite*, *ring*, *bar*, or *dumbbell* types as far as it collapses. The parameter $\Omega_0 t_{\rm ff}$ solely specifies whether the cloud fragments, whereas the other parameters specify only the type of fragmentation.

4.2.1. Ring type fragmentation

Ring type fragmentation takes place in models with large C and small $\Omega_2 t_{\rm ff}$. A ring forms during the collapse and fragments into more than three fragments.

Figure 20 show the model with ($\Omega_0 t_{\rm ff}$, $\Omega_2 t_{\rm ff}$, C) = (0.2, 0.0, 1.0) as a typical model of *ring* type fragmentation. Figure 20*a* shows the central cloud at the end of the isothermal collapse phase. The evolution is similar for *ring* type and *ring-bar* type as far as the isothermal collapse phase is concerned, with a flat disk forming in the cloud center. Figure 20*b* shows the stage of $t - t_{\rm cr} = 634$ yr. The central disk suffers from ring instability, and the ring is more prominent than for the *ring-bar* type. Figure 20*c* shows the stage of $t - t_{\rm cr} = 879$ yr, just at the moment of fragmentation. The ring fragments directly into four fragments, whereas the ring deforms into a bar before fragmentation in *ring-bar* type fragmentation. Figure 20*d* shows the stage of $t - t_{\rm cr} = 1.26 \times 10^3$ yr (the last stage), in which four fragments can be seen. The loci of the four fragments are shown in Figure 21. The two central fragments (blue and red) exhibit close encounter while the outer fragments (green and purple) rotate with wide orbits. At the last stage, the masses of the fragments are $M_{13} = 2.0 \times 10^{-2} M_\odot$ (red), $9.4 \times 10^{-3}\, M_\odot$ (blue), $7.0 \times 10^{-3}\, M_\odot$ (green), and $7.4 \times 10^{-3}\, M_\odot$ (purple). The calculation was terminated here because the Jeans condition was violated after the escape of the outer fragments from the fine grid at $l = 12$.

4.2.2. Bar type fragmentation

Bar type fragmentation takes place in models with large $\Omega_2 t_{\rm ff}$. The cloud collapses to form a narrow bar. Although the bar fragments into two fragments in many models, the fragments in this model merge to form a central adiabatic core. The merger is due to the small angular momentum of the fragments. After the merger, the adiabatic core excites spiral arms and eventually *satellite* type fragmentation occurs as shown in §4.1.4. Figure 22 shows the model with ($\Omega_0 t_{\rm ff}$, $\Omega_2 t_{\rm ff}$, C) = (0.2, 0.2, 0.15) as a typical model of *bar* type fragmentation followed by *satellite* type fragmentation.

Figure 22*a* shows the cloud at the end of the isothermal collapse phase, where it collapses to form a dense bar. Figure 23 shows the evolution of the eccentricity, flatness and rotation of the central part of the cloud in the isothermal collapse phase. The central angular velocity in unit freefall time, $\Omega_{0.5} t_{\rm ff}$ and $\Omega_{0.1} t_{\rm ff}$, increases in proportion to $n_{\rm max}^{1/6}$ and reaches $\Omega_{0.5} t_{\rm ff} = 0.460$ at $n_{\rm max} = 9.04 \times 10^7\,{\rm cm}^{-3}$ and $\Omega_{0.1} t_{\rm ff} = 0.291$ at $n_{\rm max} = 1.14 \times 10^8\,{\rm cm}^{-3}$. Meanwhile, the cloud collapses almost spherically. During $n_{\rm max} > 10^8\,{\rm cm}^{-3}$, $\Omega t_{\rm ff}$ decreases, and the flatness increases in proportion to $n_{\rm max}^{1/2}$ and exceeds unity at $n_{\rm max} \simeq 10^8\,{\rm cm}^{-3}$. The eccentricity also increases, although with significant oscillation. At the end of the isothermal collapse phase, a_l, a_s, and a_z are 56.0 AU, 18.4 AU, and 3.84 AU, respectively. The long axis a_l is 3.05 times longer than the short axis a_s.

Figure 22*b* shows the central cloud at $t - t_{\rm cr} = 210$ yr. The bar-shaped, adiabatic core

is surrounded by the isothermal disk. At this stage, a_l, a_s, and a_z are 30.4 AU, 2.80 AU, and 2.99 AU, respectively. The long axis a_l is 10.9 times longer than the short axis a_s.

Figure 22*c* shows the fragmentation of the narrow adiabatic bar at $t - t_{\rm cr} = 510$ yr. The bar is wound due to the differential rotation, and develops two density peaks. The separation between these peaks is 12.0 AU. Figure 22*d* shows the cloud at $t - t_{\rm cr} = 1.01 \times 10^3$ yr. These density peaks merge to form a central core surrounded by an adiabatic disk with spiral arms. The spiral arms are the remnants of the wound bar. The disk is supported by centrifugal force and its radius is approximately 20 AU at this stage. The disk radius increases due to the accretion of gas from the infalling envelope, and by $t - t_{\rm cr} \simeq 1.5 \times 10^3$ yr, the disk has a radius of ~ 40 AU and deforms into a ring. The ring is connected to the central kernel via the spiral arms, and the three satellite fragments form at the intersections of the ring and the spiral arms, as shown in Figure 22*e*.

Figure 22*f* shows the stage of $t - t_{\rm cr} = 1.25 \times 10^3$ yr (the last stage), in which five fragments can be seen. One of the two central fragments is formed by subsequent *satellite* type fragmentation. These fragments rotate in a close orbit of 17.1 AU. The masses of the fragments of the tight binary at the center are $M_{13} = 1.6 \times 10^{-2}\,M_\odot$ and $1.7 \times 10^{-2}\,M_\odot$. The masses of the other fragments are $M_{13} = 9.4 \times 10^{-3}\,M_\odot$, $5.8 \times 10^{-3}\,M_\odot$, and $1.8 \times 10^{-3}\,M_\odot$ from inner to outer.

4.2.3. Dumbbell type fragmentation

Dumbbell type fragmentation takes place in models with large $\Omega_2 t_{\rm ff}$ and large C. The cloud collapses to form a dumbbell-shaped dense cloud having two density peaks at the end of the isothermal collapse phase. The dumbbell shape is a hybrid of the ring and bar forms. Although each of the density peaks evolves into a fragment, the fragments often merge as in *bar* type fragmentation. *Satellite* fragments form at a later stage whenever *dumbbell* type fragmentation occurs.

Figure 24 show the model of $(\Omega_0 t_{\rm ff}, \Omega_2 t_{\rm ff}, C) = (0.2, 0.2, 0.5)$, as a typical model of *dumbbell* type fragmentation followed by *satellite* type fragmentation. The evolution of *dumbbell* type fragmentation is similar to that of *bar* type fragmentation. Figure 24*a* shows the dense dumbbell-shaped cloud at the beginning of the accretion phase ($t - t_{\rm cr} = 151$ yr). The two density peaks evolve into self-gravitationally bounded fragments, as shown in Figure 24*b* ($t - t_{\rm cr} = 673$ yr), surrounded by the isothermal disk. The fragments then merge to form a central kernel. Figure 25 shows the loci of the fragments during the merger.

After the merger, the evolution of *dumbbell* type fragmentation is very similar to that

of *bar* type. The central kernel is surrounded by a rotation-supported disk, which grows in radius by the accretion of gas from the infalling envelope. Figure 24*c* shows the disk at $t - t_{\rm cr} = 1.03 \times 10^3$ yr. The disk radius increases to $\simeq 40$ AU at this stage and deforms into a ring. Figure 24*d* shows the last stage. Satellite fragments form at the intersections of the ring and the spiral arms as in model shown in Figure 22*f*.

4.3. Classification of Fragmentation Processes

The seven types of collapse and fragmentation described above: *disk*, *disk-bar*, *ring-bar*, *satellite*, *ring*, *bar*, and *dumbbell* types, are summarized as a means of classification. Figure 26 shows the branching of these fragmentation types schematically. In the isothermal collapse phase, cloud collapse is classified into four main types: *disk*, *bar*, *dumbbell*, and *ring* types. *Disk* type collapse is subdivided into *disk*, *satellite*, *bar*, and *ring* in the accretion phase.

For all types, fragments (self-gravitationally confined clumps) form only in the accretion phase. The isothermal collapse phase is so short that the cloud deforms into a disk, bar, dumbbell, or ring-shape, but does not fragment.

Figure 27 summarizes domain of each type of collapse and fragmentation in three-dimensional phase space ($\Omega_0 t_{\rm ff}$, $\Omega_2 t_{\rm ff}$, C). The models with $\Omega_0 t_{\rm ff} \leq 0.03$ exhibit *disk* type collapse ($\times$) except for one model, while almost all models with $\Omega_0 t_{\rm ff} \geq 0.05$ undergo fragmentation. Some exceptional models exhibit *oscillation* ($*$). The other parameters, $\Omega_2 t_{\rm ff}$ and C, specify the type of fragmentation.

The red symbols denote the models exhibiting *satellite* type fragmentation. The red cross ($\times$) denotes the model exhibiting *disk* type collapse followed by *satellite* type fragmentation, as shown in §4.1.1. Similarly the red triangle ($\triangle$) denotes the model of *bar* type fragmentation followed by *satellite* type fragmentation. Almost all the models proceeds to *satellite* type fragmentation when the bar mode $\Omega_2 t_{\rm ff}$ of the the initial cloud is significant.

Fragmentation could not be confirmed for the models indicated by filled symbols. Almost all of these models have either a long bar, long dumbbell, or large ring in the beginning of the accretion phase. For the models indicated by filled triangles ($\blacktriangle$) and inverted triangles ($\blacktriangledown$), both the long bar and dumbbell are likely to fragment but could not be confirmed due to violation of the Jeans condition before fragmentation. From comparison with *bar* and *dumbbell* type fragmentation as shown in §4.2.2 and §4.2.3, these fragments appear to merge, and *satellite* type fragmentation should follow the merger. Similarly, for models indicated by filled circles ($\bullet$), the formation of a ring but could be followed but subsequent fragmentation cloud not.

5. Discussion

5.1. Collapse, Fragmentation, Survival, and Merger

In this subsection, the fate of the collapsing clouds is discussed in detail.

A cloud fragments whenever the cloud collapses and the initial rotation is faster than $\Omega_0 t_{\rm ff} \simeq 0.05$, independent of the other parameters Ω_2 and C. The cloud collapses to form a flat disk in the isothermal collapse phase, and fragmentation of the flat disk is occurs by *disk-bar*, *ring-bar*, *ring*, *bar*, *dumbbell*, and *satellite* types. When $\Omega_0 t_{\rm ff} \lesssim 0.05$, a flat disk forms in the accretion phase. The flat disk formed in the isothermal collapse phase fragments, whereas that formed in the accretion phase does not.

The criterion for fragmentation is given by the initial angular velocity. The critical angular velocity, $\Omega_0 t_{\rm ff} \simeq 0.05$, is evaluated in terms of spin-up of the collapsing cloud. An isothermal cloud in runaway collapse spins up in proportion to $\Omega_c t_{\rm ff} \propto \rho_c^{1/6}$, where Ω_c denotes the angular velocity at the center (Hanawa & Nakayama 1997). After the cloud changes its shape from a sphere to a disk, the angular velocity becomes saturated at $\Omega_c t_{\rm ff} \simeq 0.5$ (Matsumoto, Hanawa, & Nakamura 1997; Matsumoto & Hanawa 1999). These quantities represent a good index of disk formation.

As shown in §4, the angular velocities $\Omega_{0.5} t_{\rm ff}$ in models of *disk*, *disk-bar*, *ring-bar*, and *bar* types have maximum values of 0.0973, 0.452, 0.381, 0.460, respectively, in the isothermal collapse phase. When $\Omega_{0.5} t_{\rm ff}$ is close to 0.5 (*disk-bar*, *ring-bar*, and *bar* types), the model forms a disk in the isothermal collapse phase and fragments in the later stages. The small difference between Ω_c and $\Omega_{0.5}$ is due to differential rotation in the core. The angular velocity is considerably smaller in the rest of the models (*disk* type).

Applying these quantities, the condition for formation of a disk in the isothermal collapse phase can be evaluated as

$$\Omega_0 t_{\rm ff} \gtrsim 0.5 \left(\frac{\rho_c}{\rho_{\rm cr}} \right)^{1/6} = 0.045 \ . \tag{19}$$

This condition is consistent with the our simulations.

The formation of a flat disk in the isothermal phase depends on the rotation of the central cloud, but not on the rotation law specified by the parameter C. In the isothermal collapse phase, the central velocity and density become more important to cloud collapse as the cloud shrinks (Matsumoto et al. 1997). During the isothermal (runaway) collapse phase, the mass of the central cloud decreases if defined as the mass contained in the isodensity sphere of $\rho_{\rm max}/2$. The mass of the central cloud is only 0.01 $M_\odot$ at the end of the isothermal phase. Since fragmentation takes place in the central 0.01 $M_\odot$, the density and velocity

thereof are important. The density and velocity in the envelope have little effect on the initial fragmentation, but is involved in evolution of the fragments in the accretion phase.

In the literature, fragmentation of clouds is typically discussed in terms of the parameters α and β (e.g., Bodenheimer & Burkert 2001), which are evaluated by volume integration of energy for the entire cloud. As described in equation (5), β depends not only on the central rotation Ω_0, but also on the rotation in the envelope. As shown in our models, the epoch of flat disk formation depends solely on Ω_0 and is affected little by rotation in the envelope. Thus, the central angular velocity Ω_0, rather than β, describes the formation of the flat disk.

The cloud fragments when it satisfies the criterion of equation (19). The number of fragments and their orbital angular momentum then determines whether the fragments merge or survive. When the cloud fragments into three or more fragments, many of the fragments survive, as shown in *ring-bar*, *satellite* and *ring* types. On the other hand, when the cloud fragments into only two fragments, the fate of the fragments depends on their orbital angular momenta: fragments with high orbital angular momentum survive (e.g., *disk-bar* type), while fragments with low orbital angular momentum merge (e.g., *bar* and *dumbbell* types). In the latter case, satellite fragments form after the merger.

The orbital angular momentum of the fragment depends on the timing of deformation into the bar-shape. When the cloud deforms into a bar in the isothermal collapse phase, the bar does not have sufficient spin angular momentum to be supported by the rotation. In the isothermal collapse phase, the cloud undergoes runaway collapse and is never supported by the rotation (Saigo & Hanawa 1998). Thus, the orbital motions of the fragments are also never supported by the rotation. Furthermore, the bar loses angular momentum via gravitational torque in the accretion phase. In the model shown in §4.2.3 (*dumbbell* type), each fragment has a specific orbital angular momentum of $6.5 \times 10^{18}\,\mathrm{cm^2\,s^{-1}}$ at the stage shown in Figure 24*b*. This specific orbital angular momentum is only 20% of that required for support by rotation at $R = 20$ AU. On the other hand, when the cloud deforms into a bar in the accretion phase, the bar is supported by the rotation (e.g., *disk-bar* type). The adiabatic disk accretes gas with high specific angular momentum and is already supported by rotation prior to its fragmentation.

5.2. Comparison with Earlier Numerical Simulations

Bar and *dumbbell* type fragmentation were also seen in the numerical simulation of Boss et al. (2000). They followed the evolution of clouds having an initial Gaussian density profile by three types of approximations; isothermal equation of state, barotropic equations of state,

and the Eddington approximation of radiative transfer. The barotropic model of Boss et al. (2000) exhibits *bar* type fragmentation. The density profiles shown in their Figs. $5c$ and $5d$ are similar to those shown in Figures $22b$ and $22d$ here. Using AMR code, they followed the formation of a bar, fragmentation of the bar, and merger of the fragments. This evolution resembles that of the model shown in §4.2.2, although the initial condition is quite different. They terminated the calculation at the stage of adiabatic disk formation after the merger, and the stage of *satellite* type fragmentation was not shown. *Dumbbell* type fragmentation is also seen in their Fig. $2a$, which is quite similar to Figure $24a$ here. *Dumbbell* type fragmentation in their study was computed under the Eddington approximation.

The initial cloud of Boss et al. (2000) is defined by $\alpha = 0.26$ whereas $\alpha = 0.765$ in the present study. Their cloud was thus colder, or in other words, more massive. Despite this difference, the fragmentation is very similar. The same mechanism of deformation and fragmentation therefore appears to be valid over a wide range of α.

Satellite type fragmentation has also been seen in many other simulations (Bonnell 1994; Burkert et al. 1997; Bate et al. 2002). Bonnell (1994) followed the fragmentation in the second collapse, in which the first core collapses to form the second core. In their simulations, satellite fragments form through interaction of the spiral arms. The satellite fragments form in the same manner both in their and our simulations, even though different situations are considered. Burkert et al. (1997) followed the collapse and fragmentation of molecular cloud cores similar to this paper. They also computed the formation of satellite fragments and followed their orbits using a nested grid. It was not explicitly mentioned whether the nested grid simulation satisfies the Jeans condition. Burkert et al. (1997) and Bate et al. (2002) confirmed the result by independent simulations using an SPH code.

5.3. Application to Formation of Binary and Multiple Stars

Some observations have indicated the rotation of molecular cloud cores. Goodman et al. (1993) found that 29 of 43 molecular clouds had significant velocity gradient, corresponding to rigid rotation of $2 \times 10^{-3} < \beta < 1.4$ with typical values of $\beta \sim 0.02$. These quantities correspond to $0.047 < \Omega_0 t_{\rm ff} < 1.25$ with typical values of $\Omega_0 t_{\rm ff} \sim 0.15$ for models of $(\Omega_2 t_{\rm ff}, C) = (0, 0)$. Unfortunately, the observations were not of sufficient accuracy to specify the rotation law. Our simulations show that collapsing clouds having an initial rotation of $\Omega_0 t_{\rm ff} \gtrsim 0.05$ fragment, which is consistent with observed high binary frequency.

Molecular cloud cores have internal motion often interpreted as turbulence. The internal motion should reflect the superposition of various modes of velocity perturbations. When

the bar mode of a cloud is a significant, the cloud undergoes *satellite* type fragmentation as shown in our simulations. Therefore, *satellite* type fragmentation may be dominant. The satellite fragments merge and scatter while accreting gas. Consequently, the satellites will have various binary separations. This may explain the wide range of separation for young and main sequence binaries (e.g., Mathieu 1994).

It has recently been suggested that brown dwarfs may be formed by ejection of the seeds of stars from a parent cloud core (Reipurth & Clarke 2001; Bate et al. 2002). *Satellite* type fragmentation might be a corresponding case. In many case of *satellite* type fragmentation, three or more fragments are formed. In these multiple systems, it is possible that a close encounter will eject the fragment from the cloud center. The satellite fragment has speed of $\sim 1\,\mathrm{km\,s^{-1}}$ at the last stage of the model of $(\Omega_0 t_{\rm ff}, \Omega_2 t_{\rm ff}, C) = (0.2, 0.2, 0.15)$ (for a fragment shown in the right side of Figure 22*f*). The velocity would be reduced substantially before ejection by the gravity of the molecular cloud core. The gravitational potential is evaluated to be $\psi \approx 2c_{\rm s}^2 \ln r$, and the ejection speed would be $v_{\rm escape} \sim 1\,\mathrm{km\,s^{-1}}$. The ejected satellite fragment would have a velocity of the order of the escape speed if it exits.

6. Summary

The collapse and fragmentation of molecular cloud cores was investigated for the case that the initial cloud is almost in equilibrium, focusing on the effects of rotation speed, rotation law, and bar mode perturbation. The main results are summarized as follows.

A cloud 1.1 times denser than the critical Bonnor-Ebert sphere fragments when rotation of the initial cloud is slowly enough to allow collapse, but still significant, i.e., $\Omega_c t_{\rm ff} \gtrsim 0.05$. The latter condition gives rise to the formation of a flat disk in the isothermal collapse phase. This condition is independent of both the initial amplitude of the bar mode and the initial rotation law.

Six types of fragmentation were identified: *disk-bar*, *ring-bar*, *satellite*, *bar*, *ring*, and *dumbbell* types. The type of fragmentation depends on the initial amplitude of the bar mode and the initial rotation law. The fragments formed via *bar* or *dumbbell* types fragmentation merge due to their low angular momenta, and new fragments form via *satellite* type fragmentation. In other words, a cloud forms satellite fragments whenever the bar mode of the initial cloud is appreciable amplitude. Merger and close encounter of the satellite fragments may result in the wide range of the binary separation.

The authors thank S. Inutsuka, T. Tsuribe, and K. Saigo for valuable discussion. Numer-

ical computations were carried out on VPP5000 at the Astronomical Data Analysis Center of the National Astronomical Observatory, Japan, which is an inter-university research institute of astronomy operated by the Ministry of Education, Culture, Sports, Science and Technology, Japan (MEXT). This study was financially supported in part by Grants-in-Aid for the Encouragement of Young Scientists (12740123, 14740134), for Scientific Research on Priority Areas (A) (13011204) from MEXT, and for Scientific Research (C) (13640237) from the Japan Society of Promotion of Science (JSPS),

REFERENCES

Alves, J., Lada, C. J., & Lada, E. A. 2001, Nature, 409, 159

Bate, M. R., Bonnell, I. A., & Bromm, V. 2002, MNRAS, 332, L65

Bodenheimer, P., Burkert, A., Klein, R. I., & Boss, A. P. 2000, Protostars and Planets IV, 675

Bodenheimer, P. & Burkert, A. 2001, IAU Symposium, 200, 13

Bonnell, I. A. 1994, MNRAS, 269, 837

Bonnor, W. B. 1956, MNRAS, 116,351

Boss, A. P. & Myhill, E. A. 1995, ApJ, 451, 218

Boss, A. P., Fisher, R. T., Klein, R. I. & McKee, C. F. 2000, ApJ, 528, 325

Boss, A. P. 1993, ApJ, 410, 157

Burkert, A., Bate, M. R., & Bodenheimer, P. 1997, MNRAS, 289, 497

Chiang, Y., van Leer, B., & Powell, K. G. 1992, AIAA Paper 92-0443, AIAA 30th Aerospace Sciences Meeting

Ebert, R. 1955, Z. Astrophys., 37, 222

Goodman, A. A., Benson, P. J., Fuller, G. A., & Myers, P. C. 1993, ApJ, 406, 528

Hanawa, T. & Matsumoto, T. 1999, ApJ, 521, 703

Hanawa, T. & Nakayama, K. 1997, ApJ, 484, 238

Harvey, D. W. A., Wilner, D. J., Lada, C. J., Myers, P. C., Alves, J. ;., & Chen, H. 2001, ApJ, 563, 903.

Hirsch, C. 1990, Numerical Computation, of Internal and External Flows, Vol. 2 (Chichester: Wiley)

Klapp, J. & Sigalotti, L. D. 1998, ApJ, 504, 158

Larson, R. B. 1969, MNRAS, 145, 271

Masunaga, H., Miyama, S. M., & Inutsuka, S. 1998, ApJ, 495, 346.

Mathieu, R. D. 1994, ARA&A, 32, 465

Matsumoto, T. & Hanawa, T. 1999, ApJ, 521, 659

Matsumoto, T. & Hanawa, T. 2003, ApJ, 583, 296

Matsumoto, T., Hanawa, T. & Nakamura, F. 1997, ApJ, 478, 569

Miyama, S. M., Hayashi, C., & Narita, S. 1984, ApJ, 279, 621

Nelson, R. P. 1998, MNRAS, 298, 657

Onishi, T., Mizuno, A., Kawamura, A., Ogawa, H., & Fukui, Y. 1996, ApJ, 465, 815

Racca, G., Gómez, M., & Kenyon, S. J. 2002, AJ, 124, 2178

Reipurth, B. & Clarke, C. 2001, AJ, 122, 432

Roe, P. L. 1981, J. Comput. Phys. 43, 357

Saigo, K. & Hanawa, T. 1998, ApJ, 493, 342

Saigo, K., Hanawa, T. & Matsumoto, T. 2002, ApJ in press

Sigalotti, L. D. 1998, ApJ, 498, 236

Tohline, J. E. 1981, ApJ, 248, 717

Toomre, A. 1964, ApJ, 139, 1217

Truelove, J. K., Klein, R. I., McKee, C. F., Holliman, J. H., Howell, L. H. & Greenough, J. A. 1997, ApJ, 489, L179

Tsuribe, T. & Inutsuka, S. 1999, ApJ, 523, L155

Yorke, H. W., Bodenheimer, P. & Laughlin, G. 1993, ApJ, 411, 274

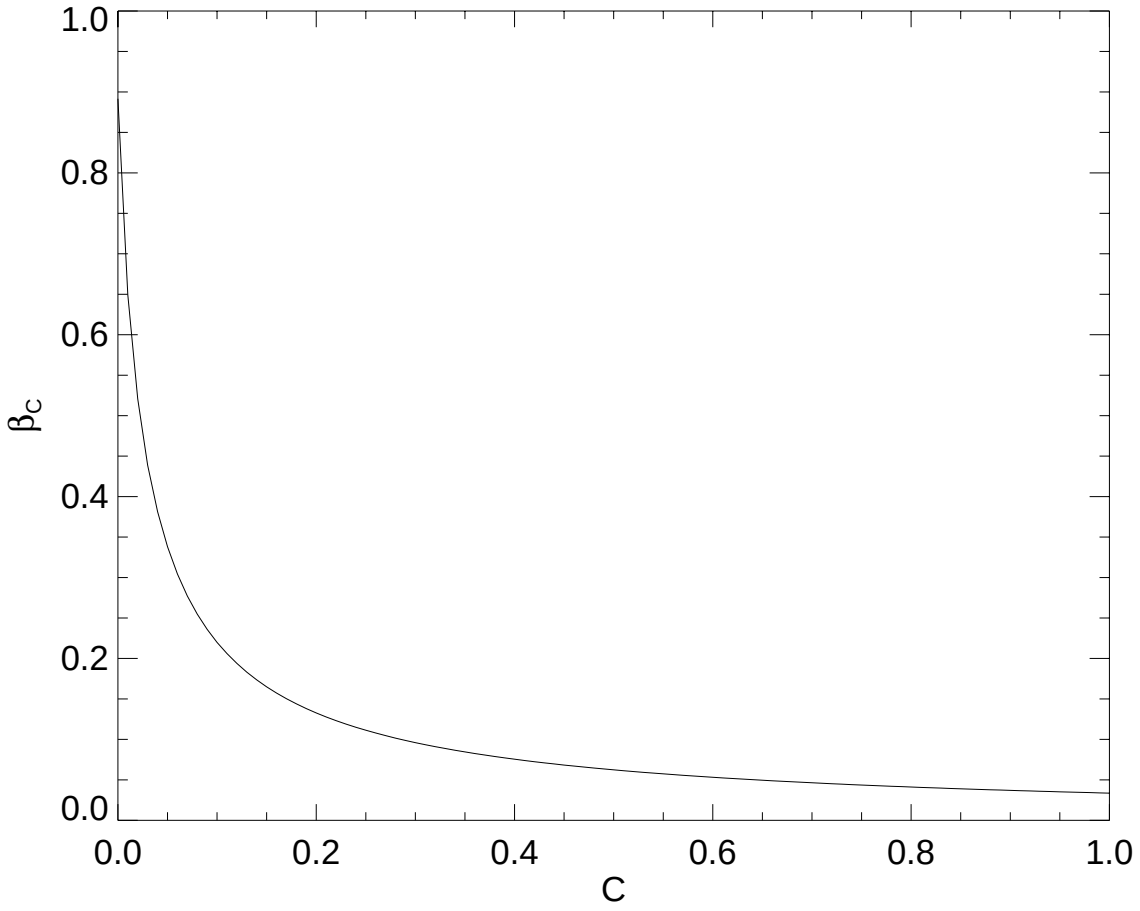

Fig. 1.— Coefficient β_C as a function of C.

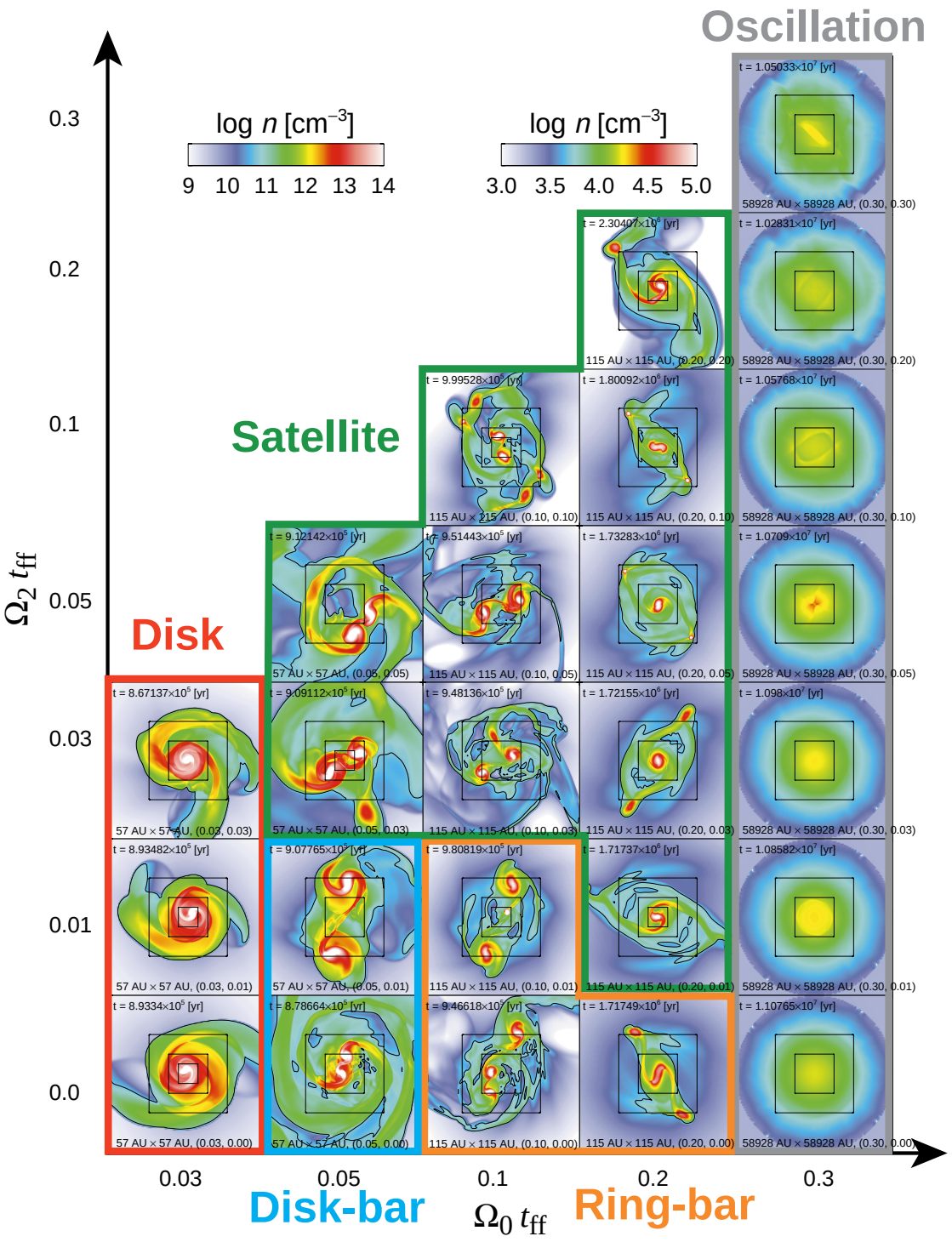

Fig. 2.— Density distributions in the $z = 0$ plane at the last stages for models of $C = 0$. Color denotes the density distribution on a logarithmic scale. The right color scale is for *oscillation* models, and the left color scale is for models of *disk*, *satellite*, *ring-bar*, and *disk-bar* types. Black contour curves denote the critical density $n_{\rm cr}$. Panels are arranged in the order of $\Omega_0 t_{\rm ff} = 0.03$, 0.05, 0.1, 0.2, 0.3 from left to right, and $\Omega_2 t_{\rm ff} = 0.0$, 0.01, 0.03, 0.05, 0.1, 0.2, 0.3 from bottom to top.

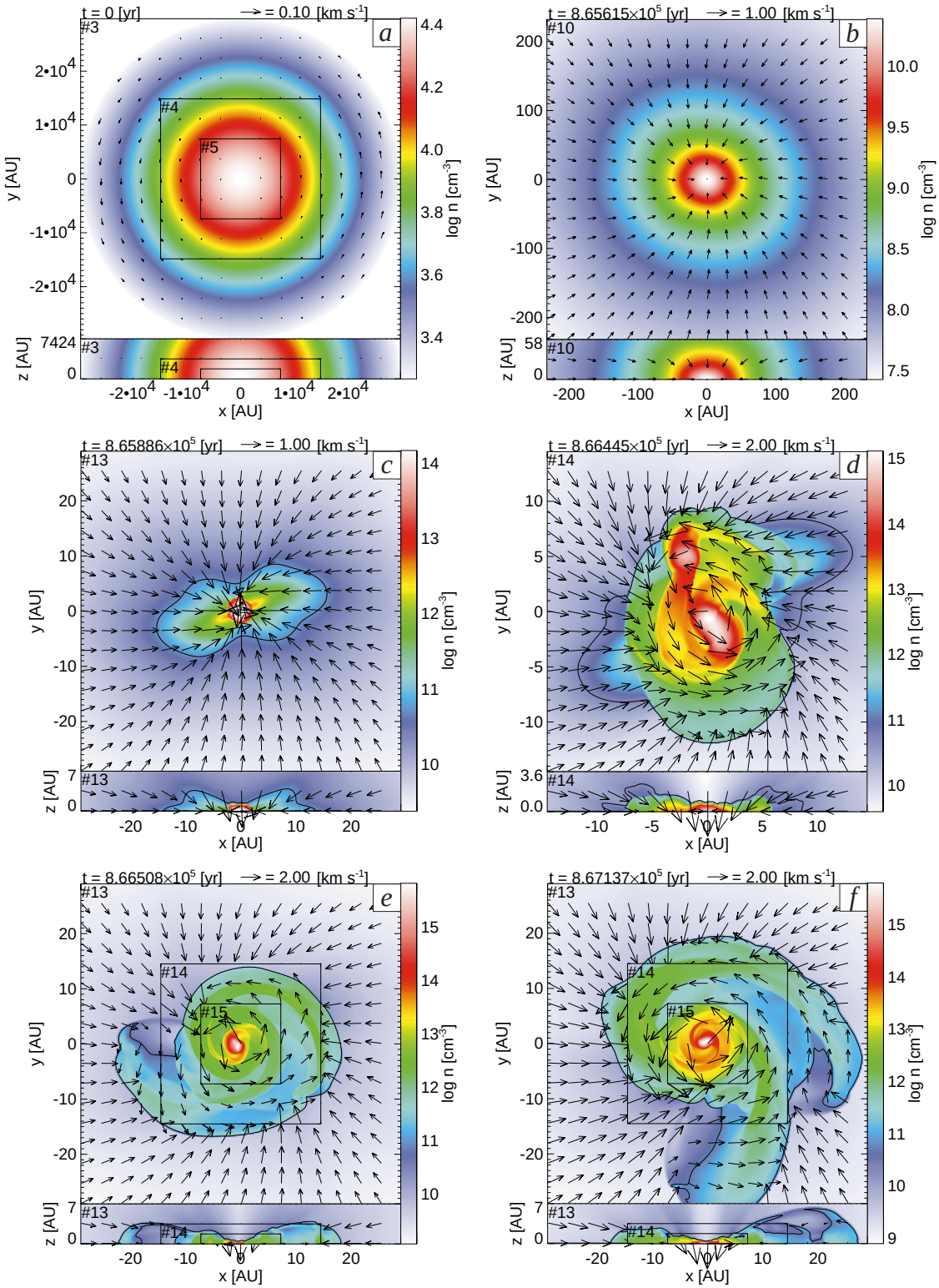

Fig. 3.— Density and velocity distributions for a model of *disk* type collapse, $(\Omega_0 t_{\rm ff}, \Omega_2 t_{\rm ff}, C) = (0.03, 0.03, 0.0)$. Upper and lower panels show the cross sections in the $z = 0$ and $y = 0$ planes, respectively. Color scale denotes the density distribution on a logarithmic scale. Contour curves denote the critical density $n_{\rm cr}$. Arrows denote the velocity.

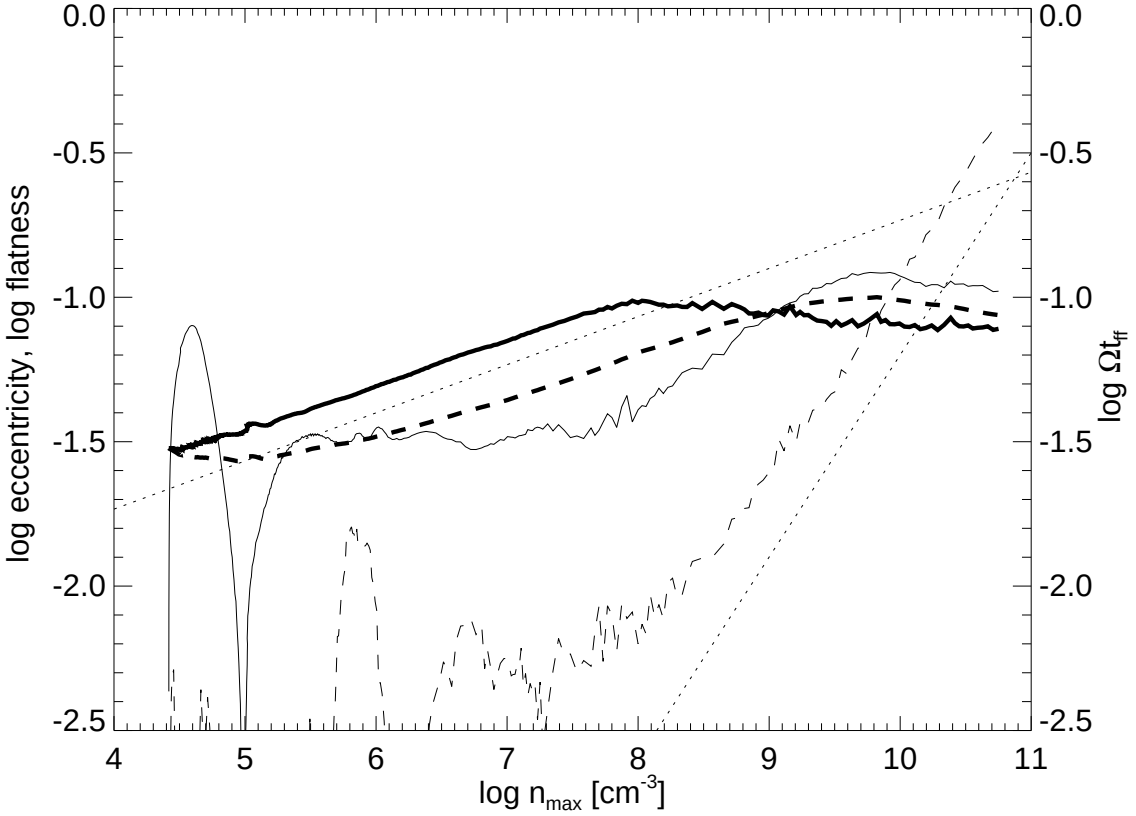

Fig. 4.— Eccentricity, flatness, and angular velocity of the dense region in the isothermal collapse phase as a function of maximum density for a model of *disk* type collapse, ($\Omega_0 t_{\rm ff}$, $\Omega_2 t_{\rm ff}$, C) = (0.03, 0.03, 0.0). Thin solid and dashed curves denote eccentricity, $a_l/a_s - 1$, and flatness, $(a_l a_s)^{1/2}/a_z - 1$, respectively. Thick solid and thick dashed curves denote angular velocities in a unit of freefall time, $\Omega_{0.5} t_{\rm ff}$ and $\Omega_{0.1} t_{\rm ff}$, respectively. Dotted curves denote the relationships $\propto n_{\rm max}^{1/6}$ and $n_{\rm max}^{0.7}$ for comparison.

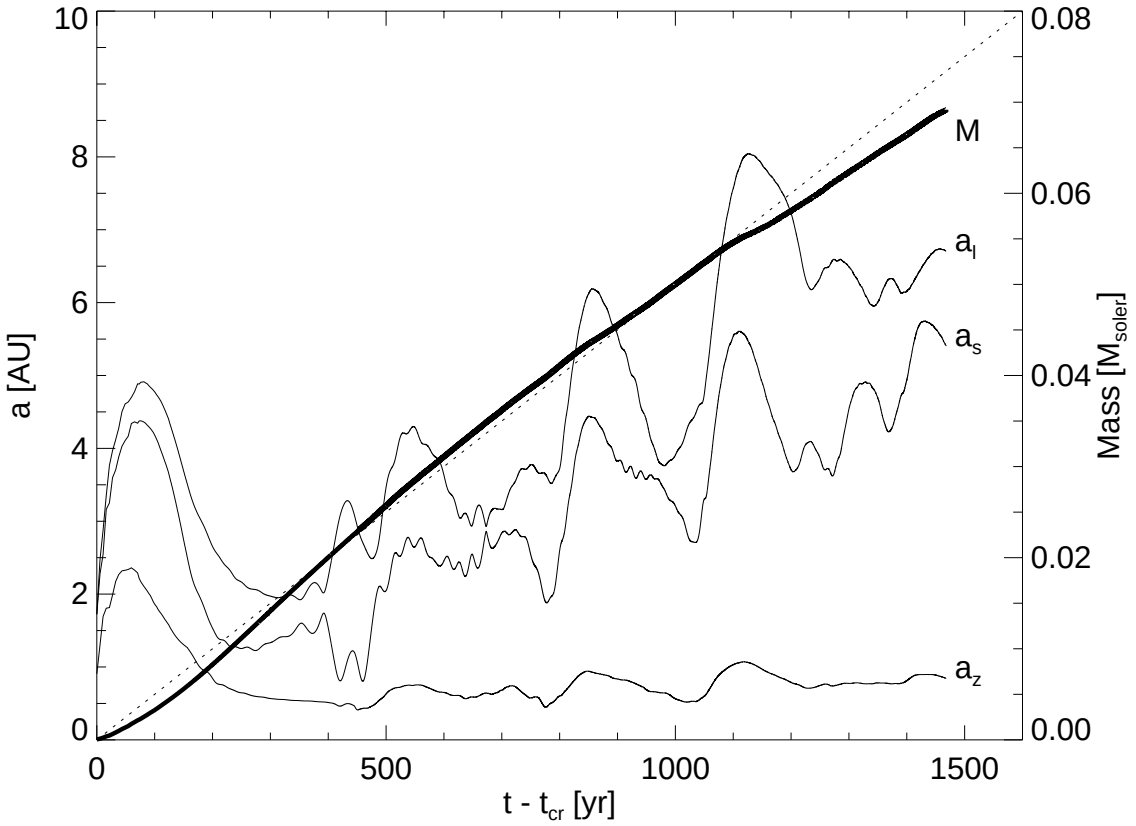

Fig. 5.— Size of the adiabatic core and mass in the accretion phase as a function of time for a model of *disk* type collapse, $(\Omega_0 t_{\rm ff},\ \Omega_2 t_{\rm ff},\ C) = (0.03,\ 0.03,\ 0.0)$. The three thin curves denote a_l, a_s, and a_z, the thick curve denotes the mass, and the dotted line denotes $M = 5 \times 10^{-5}(t - t_{\rm cr})\, M_\odot\, {\rm yr}^{-1}$ for comparison.

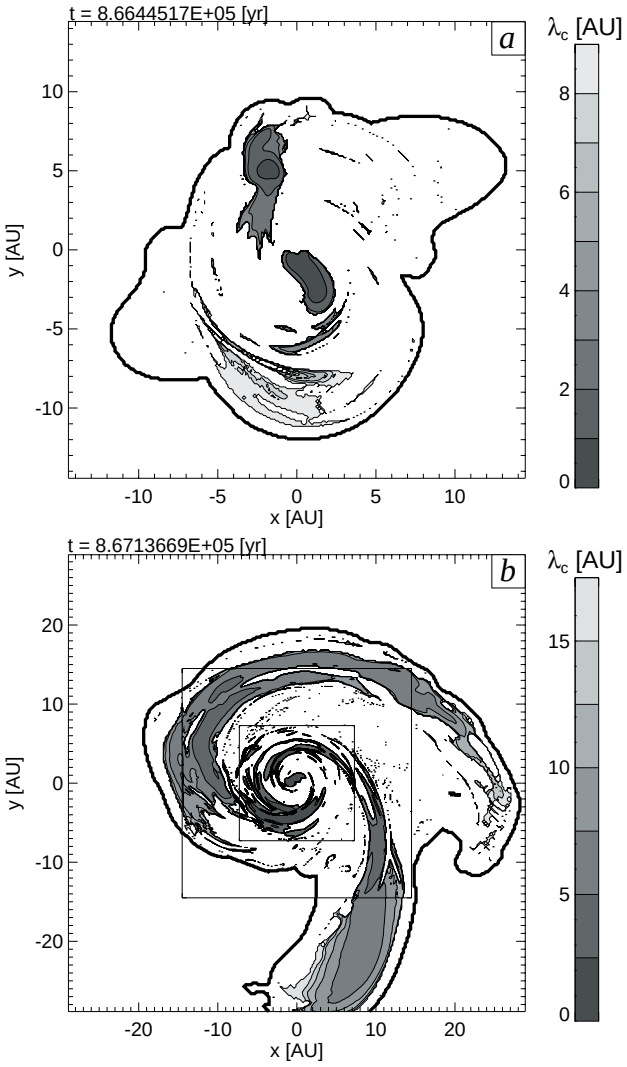

Fig. 6.— Distribution of the critical Jeans length λ_c for a model of *disk* type collapse, ($\Omega_0 t_{\rm ff}$, $\Omega_2 t_{\rm ff}$, C) = (0.03, 0.03, 0.0). Thick contour curve denotes the outline of the adiabatic disk. The grayscale denotes the critical Jeans length λ_c. $Q > 1$ in the white region. Figures (a) and (b) correspond to the stages of Figures 3d and 3f, respectively.

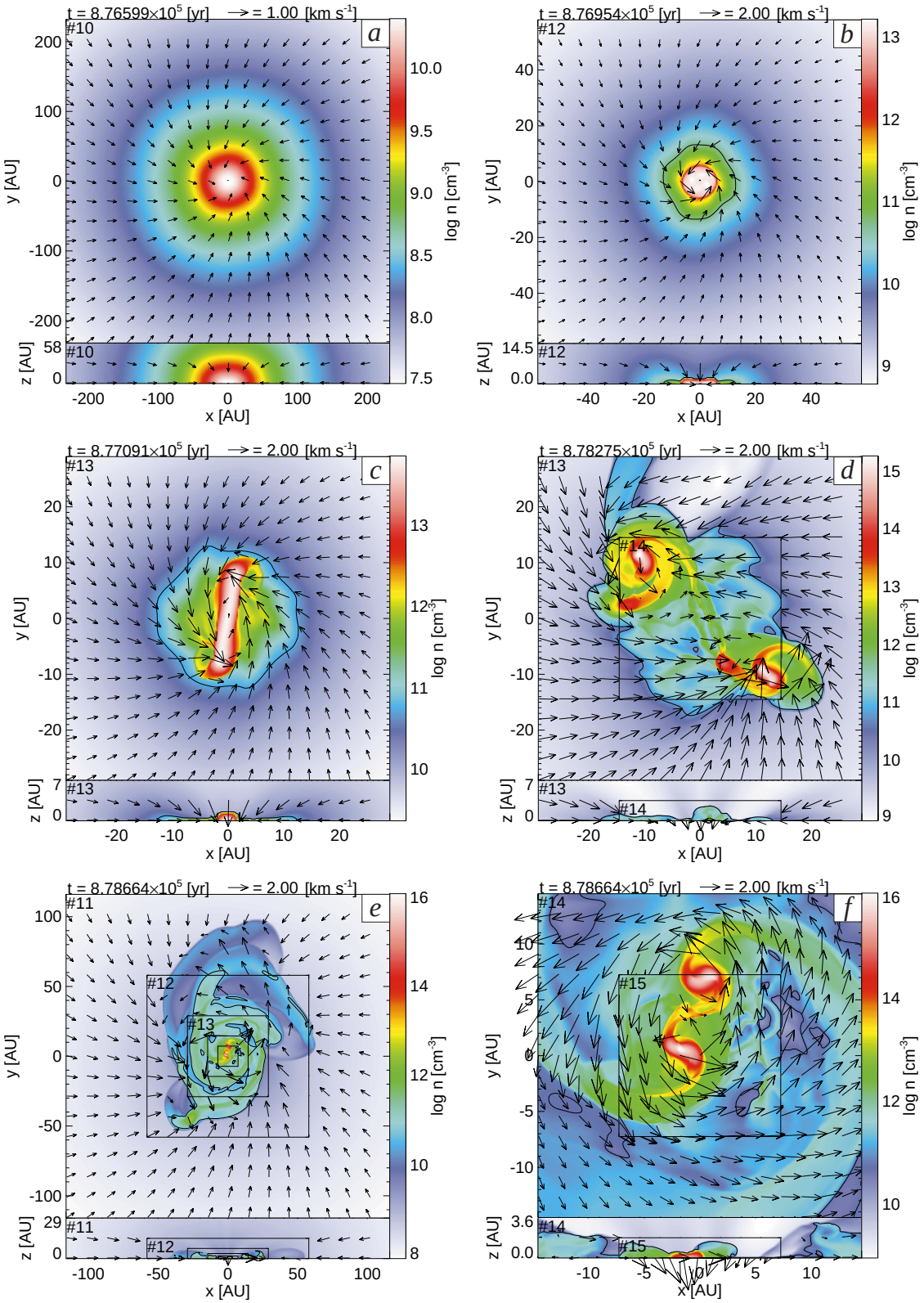

Fig. 7.— Same as Figure 3 but for a model of *disk-bar* type fragmentation, ($\Omega_0 t_{\rm ff}$, $\Omega_2 t_{\rm ff}$, C) = (0.05, 0.0, 0.0). Figure 7*f* is an enlargement of Figure 7*e*.

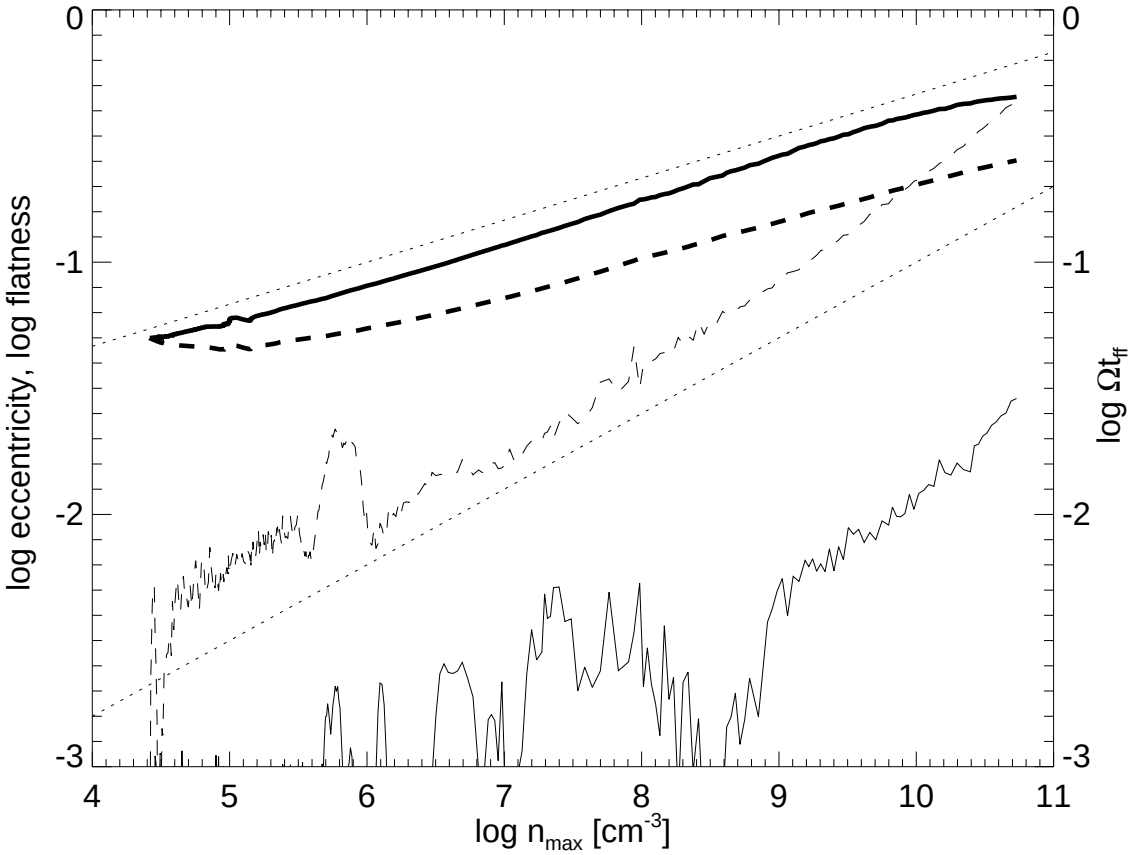

Fig. 8.— Same as Figure 4 but for a model of *disk-bar* type fragmentation, ($\Omega_0 t_{\rm ff}$, $\Omega_2 t_{\rm ff}$, C) = (0.05, 0.0, 0.0). Dotted curves denote the relationships $\propto n_{\rm max}^{1/6}$ and $n_{\rm max}^{0.3}$ for comparison.

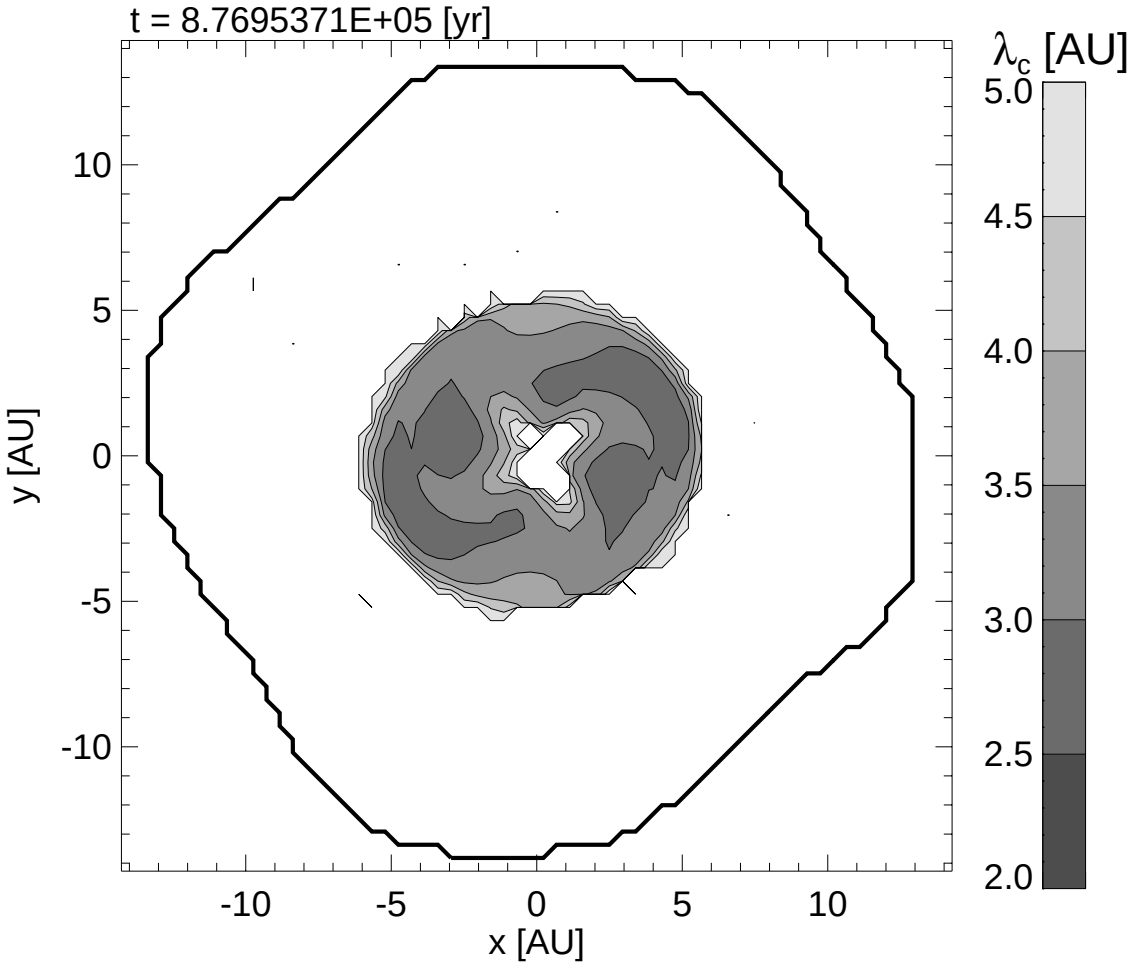

Fig. 9.— Same as Figure 6 but for a model of *disk-bar* type fragmentation, ($\Omega_0 t_{\rm ff}$, $\Omega_2 t_{\rm ff}$, C) = (0.05, 0.0, 0.0) at the same stage as in Figure 7*b*.

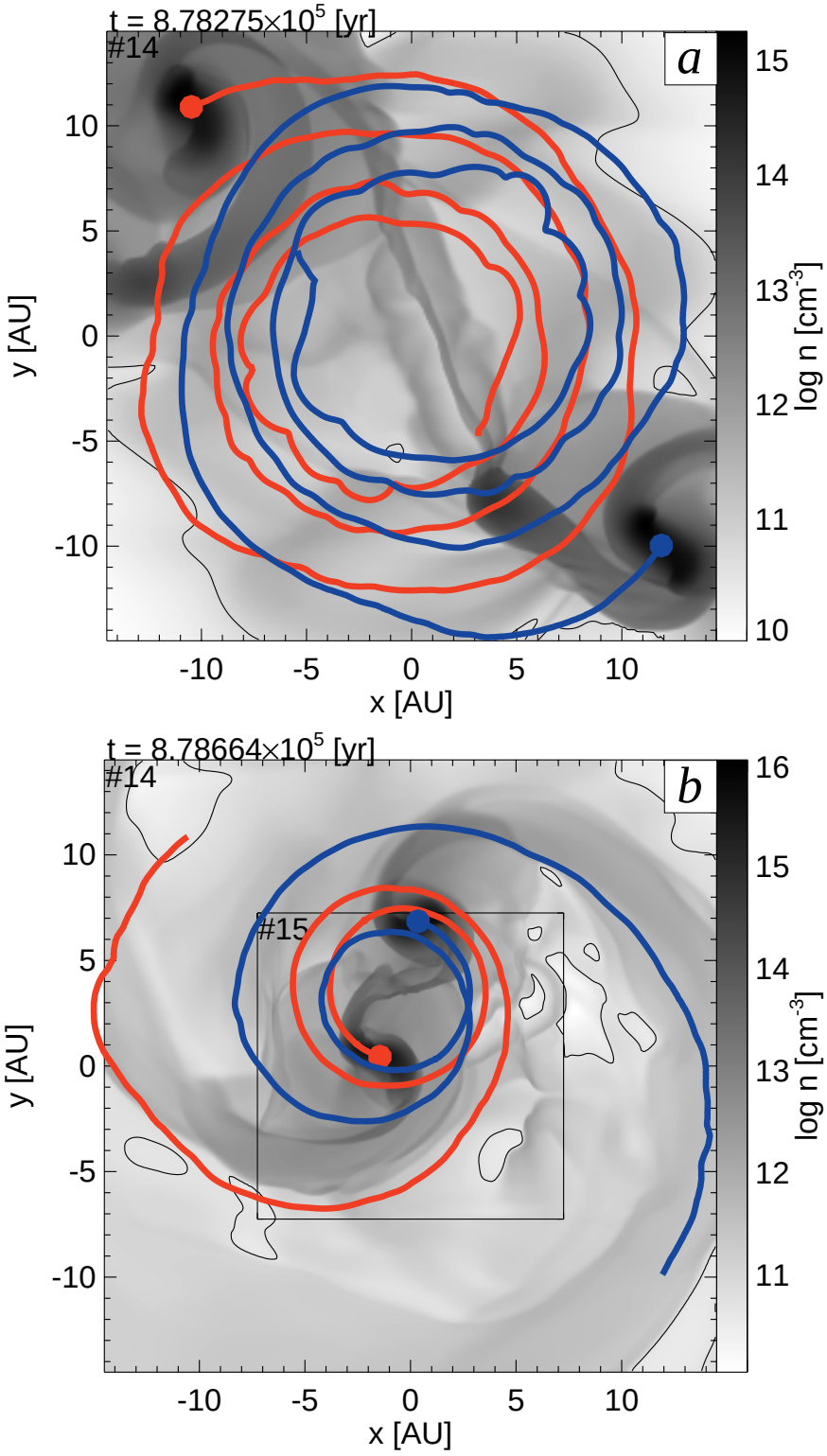

Fig. 10.— Loci of fragments in the $x-y$ plane for the model of *disk-bar* type fragmentation, $(\Omega_0 t_{\rm ff},\ \Omega_2 t_{\rm ff},\ C) = (0.05,\ 0.0,\ 0.0)$. Color curves trace the barycenters of each fragment ($n \geq 10^{14}\,{\rm cm}^{-3}$) in the period ($a$) between the stage of fragmentation and maximum separation, and (b) in the rest stages. The grayscales in figures (a) and (b) denote the density distributions at the stages of Figures 7*d* and 7*f*, respectively.

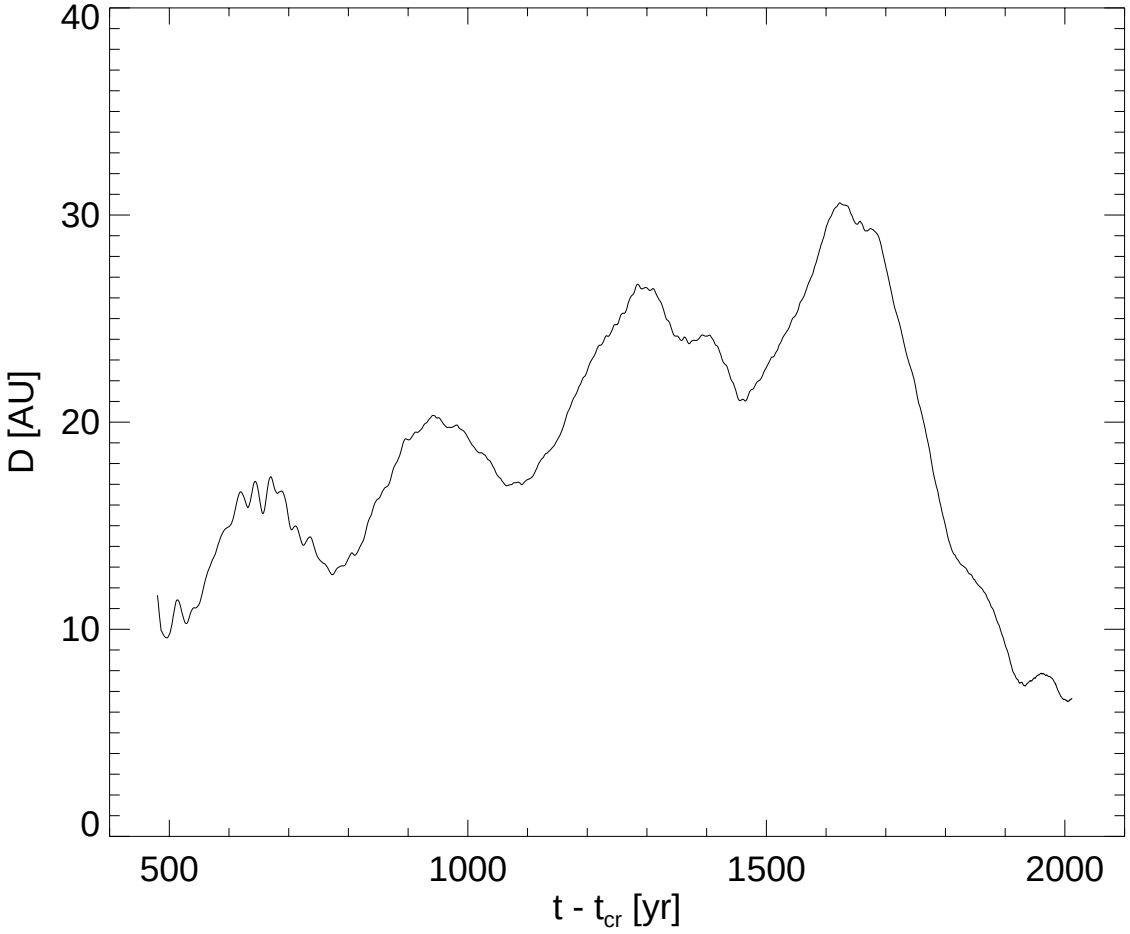

Fig. 11.— Separation between fragments as a function of time for *disk-bar* type model, ($\Omega_0 t_{\rm ff}$, $\Omega_2 t_{\rm ff}$, C) = (0.05, 0.0, 0.0).

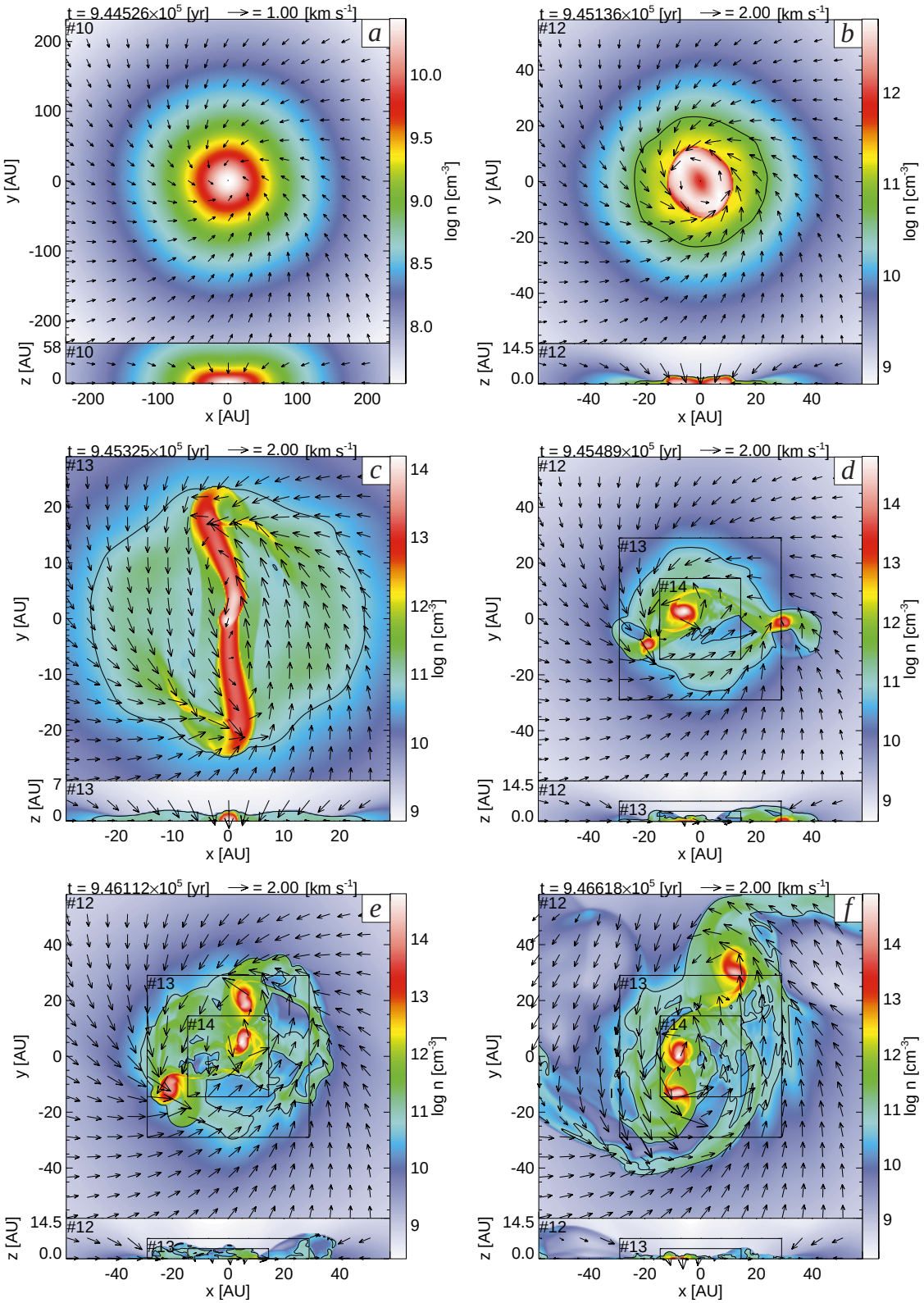

Fig. 12.— Same as Figure 3 but for a model of *ring-bar* type fragmentation, ($\Omega_0 t_{\rm ff}$, $\Omega_2 t_{\rm ff}$, C) = (0.1, 0.0, 0.0).

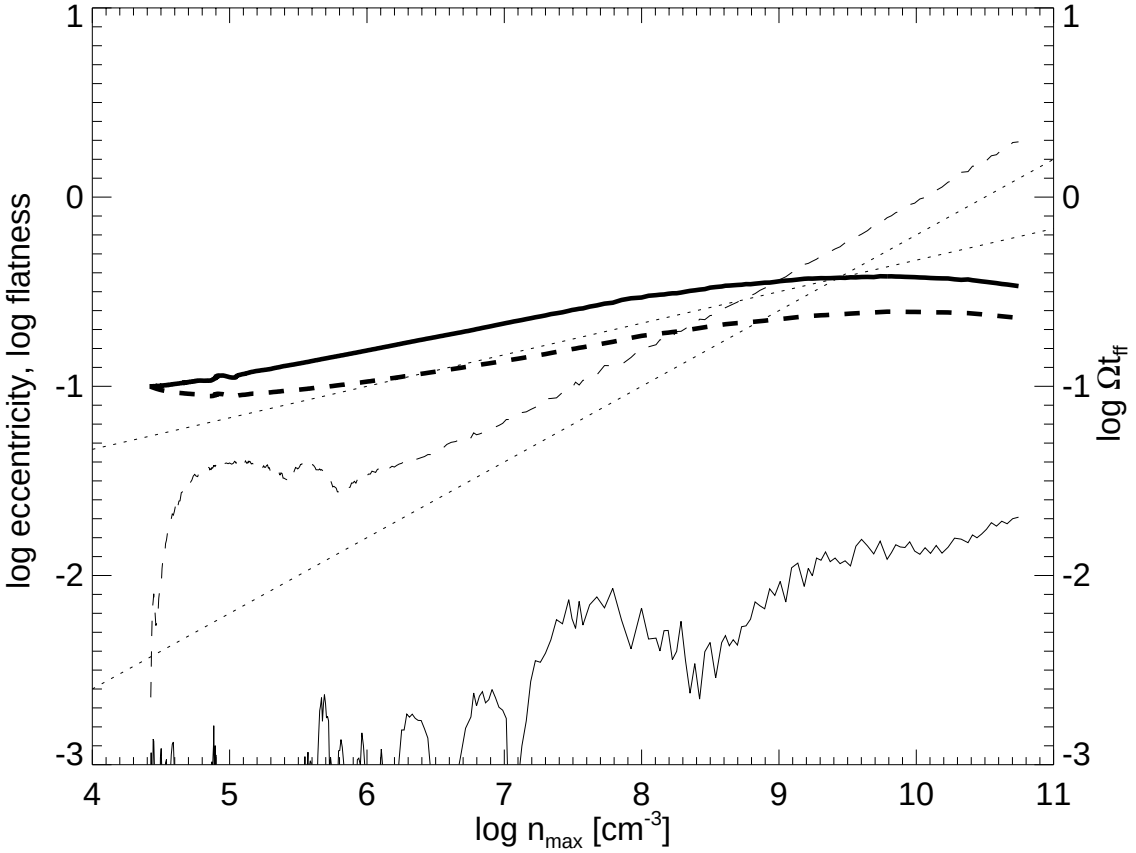

Fig. 13.— Same as Figure 4 but for a model of *ring-bar* type fragmentation, ($\Omega_0 t_{\rm ff}$, $\Omega_2 t_{\rm ff}$, C) = (0.1, 0.0, 0.0). Dotted curves denote the relationships $\propto n_{\rm max}^{1/6}$ and $n_{\rm max}^{0.4}$ for comparison.

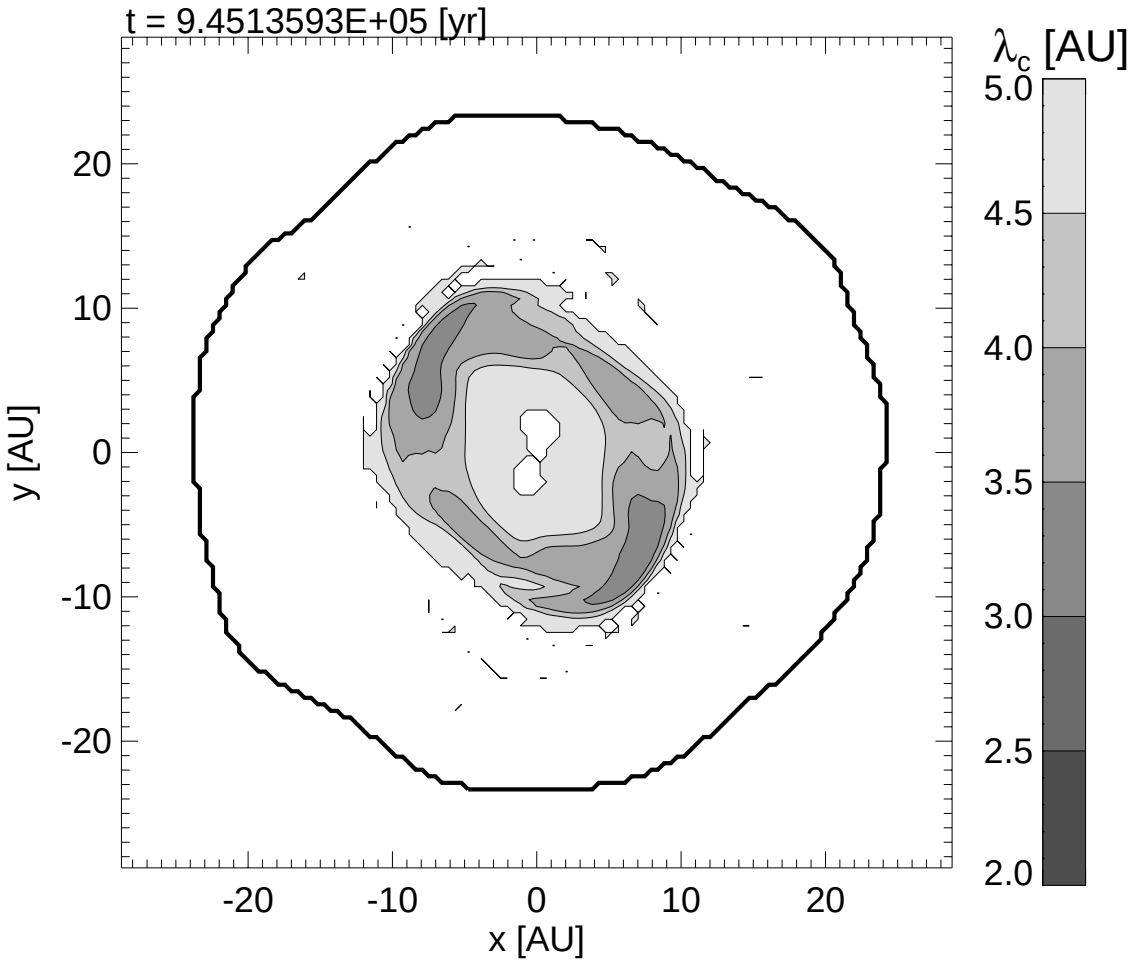

Fig. 14.— Same as Figure 6 but for a model of *ring-bar* type fragmentation, ($\Omega_0 t_{\rm ff}$, $\Omega_2 t_{\rm ff}$, C) = (0.1, 0.0, 0.0) at the same stage as in Figure 12*b*.

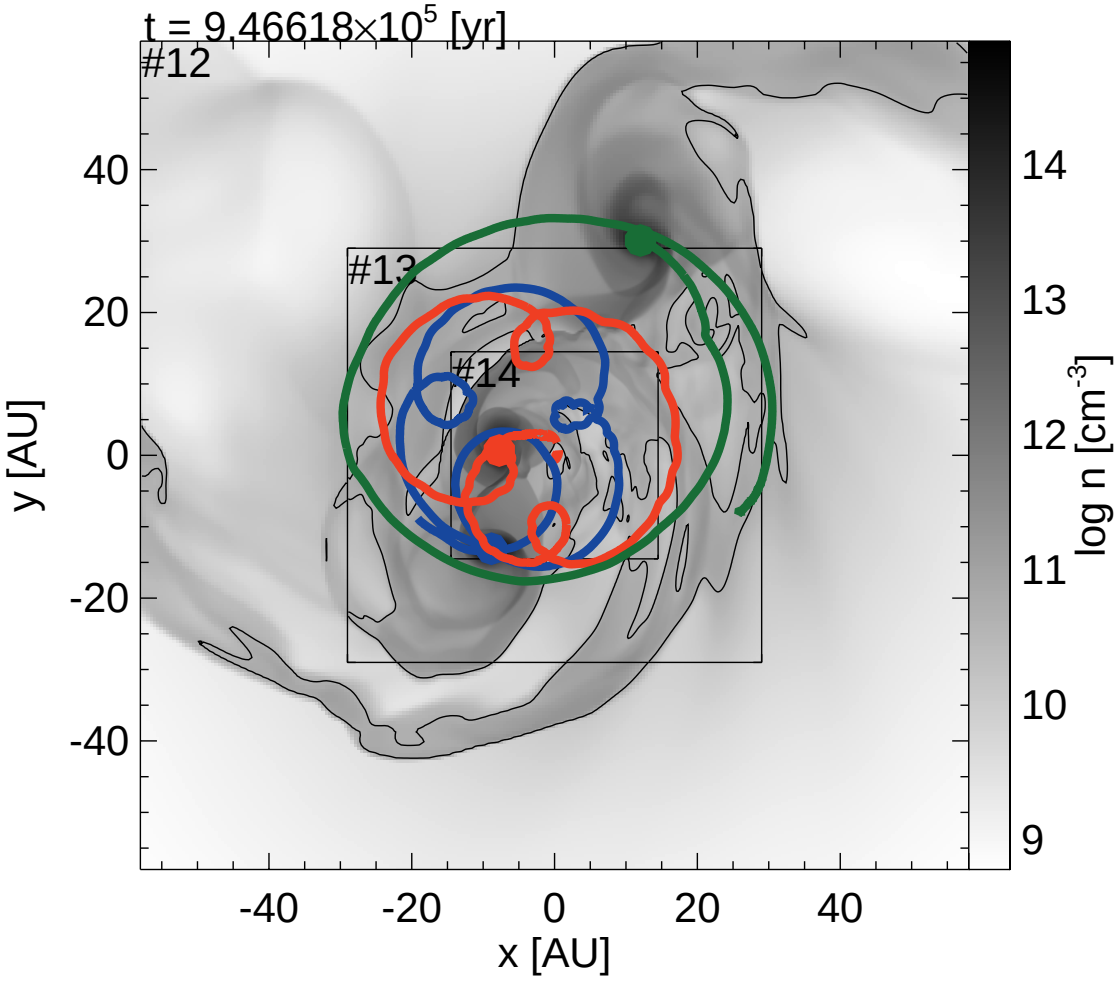

Fig. 15.— Same as Figure 10 but for a model of *ring-bar* type fragmentation, $(\Omega_0 t_{\rm ff}, \Omega_2 t_{\rm ff}, C)$ = (0.1, 0.0, 0.0). Red and blue loci trace the barycenters of each fragment of $n \geq 10^{14}\,{\rm cm}^{-3}$. Green locus is for the fragment of $n \geq 10^{13}\,{\rm cm}^{-3}$. Grayscale denotes the logarithmic density at the same stage as in Figure 12*f*.

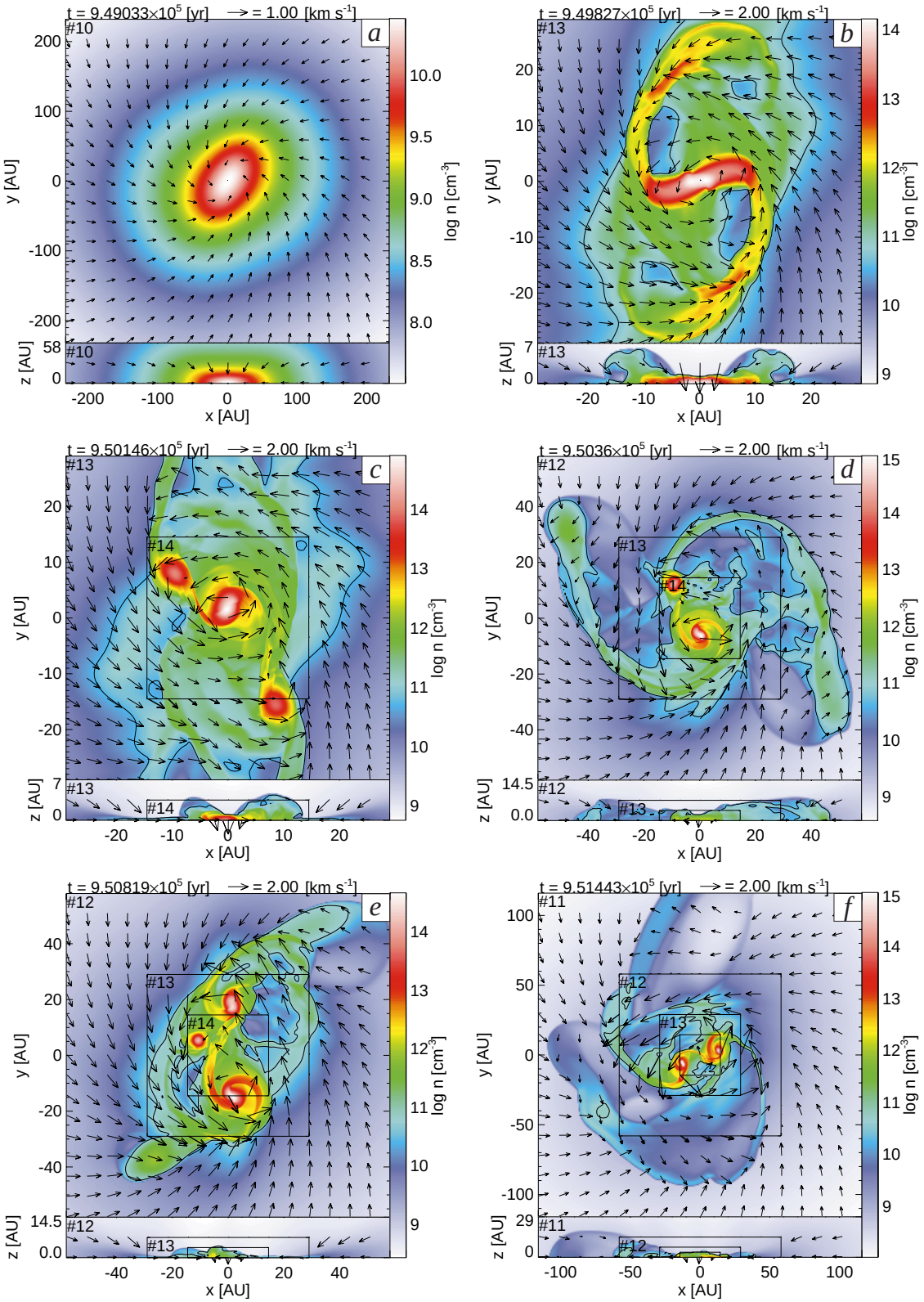

Fig. 16.— Same as Figure 3 but for a model of *satellite* type fragmentation, ($\Omega_0 t_{\rm ff}$, $\Omega_2 t_{\rm ff}$, C) = (0.1, 0.05, 0.0).

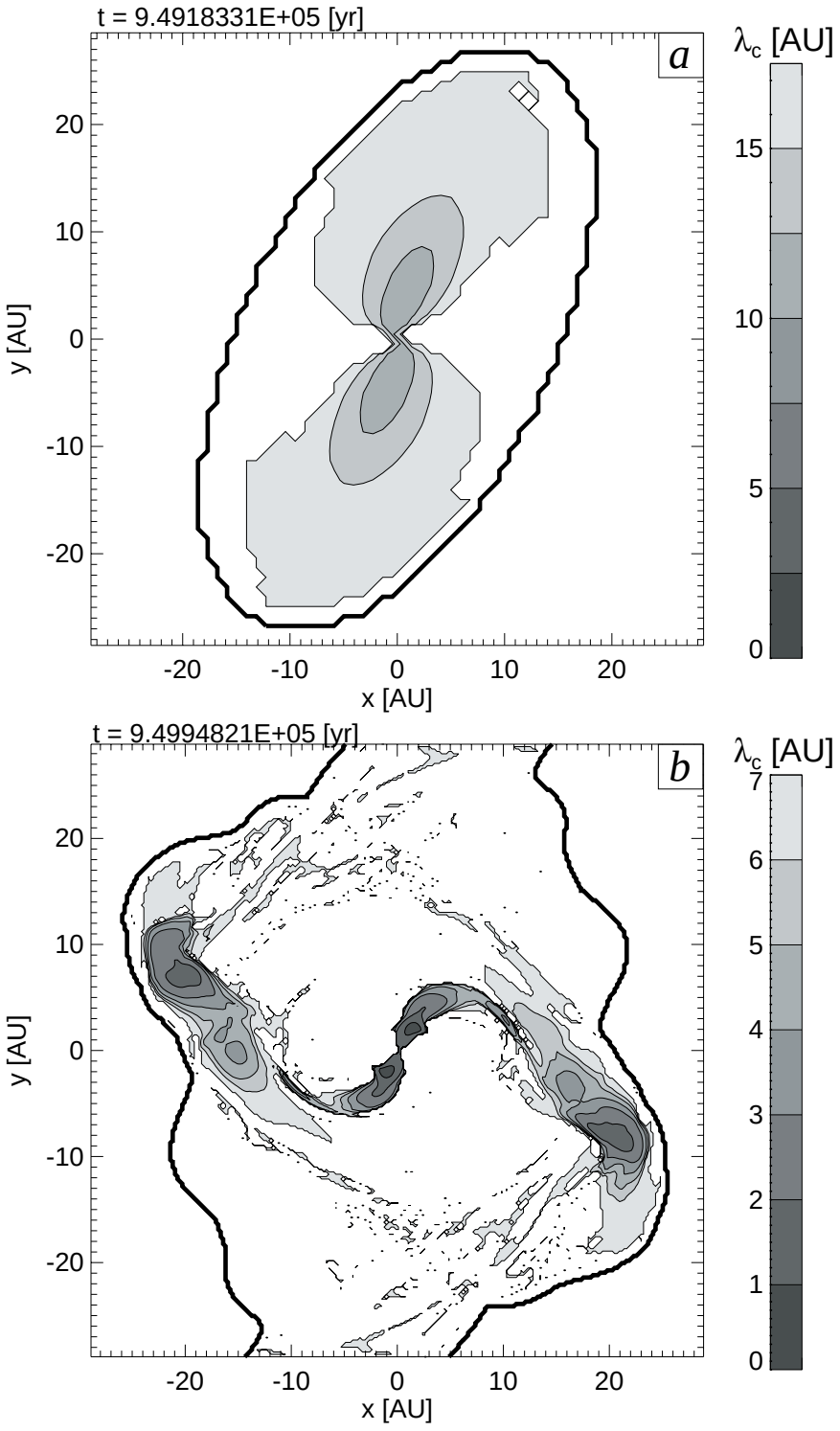

Fig. 17.— Same as Figure 6 but for a model of *satellite* type fragmentation, ($\Omega_0 t_{\rm ff}$, $\Omega_2 t_{\rm ff}$, C) = (0.1, 0.05, 0.0).

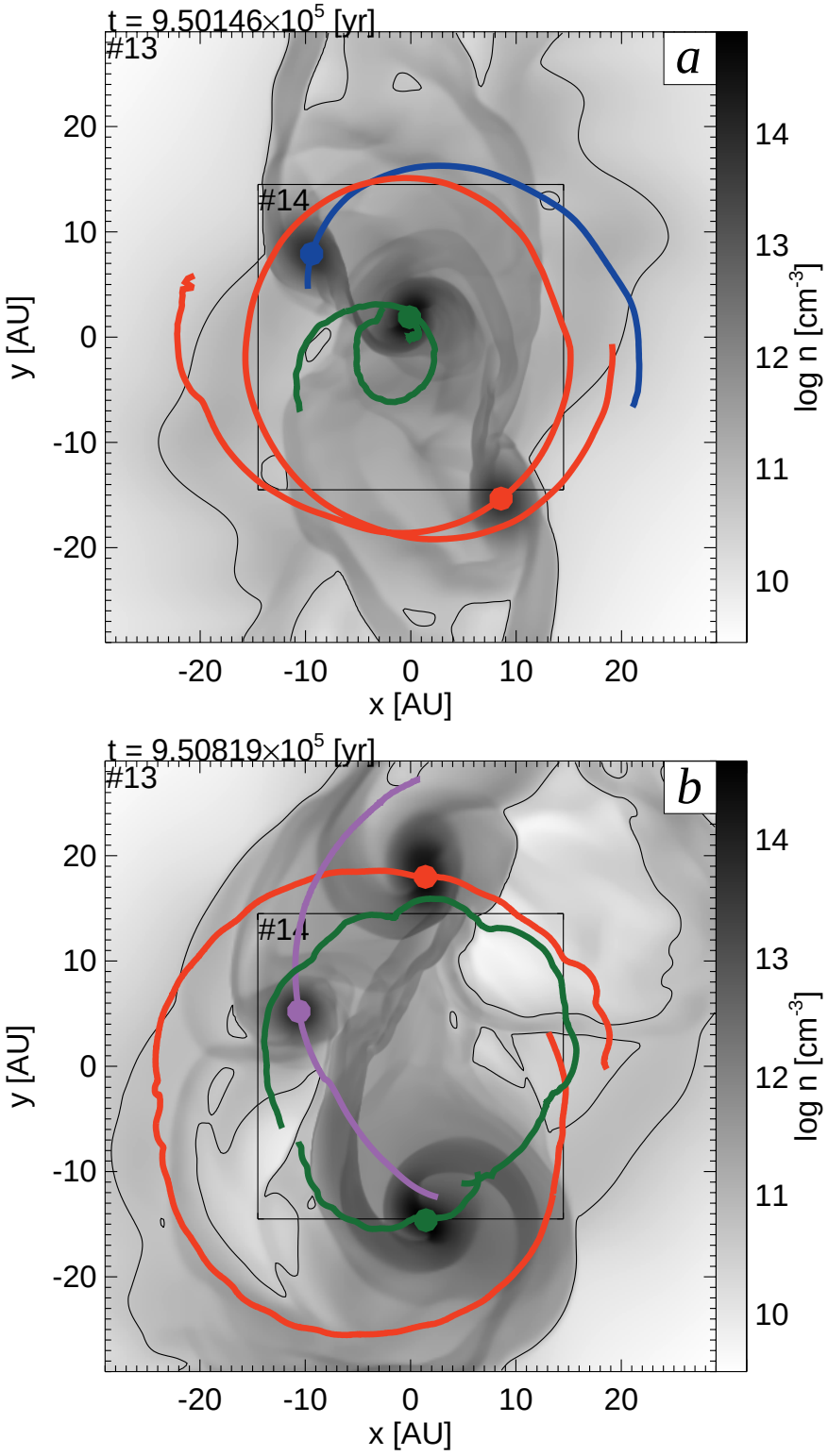

Fig. 18.— Same as Figure 10 but for a model of *satellite* type fragmentation, $(\Omega_0 t_{\rm ff}, \Omega_2 t_{\rm ff}, C) = (0.1, 0.05, 0.0)$. Colored curves trace the barycenters of (a) each fragment of $n \geq 10^{13}\,{\rm cm}^{-3}$ in the period between the stages of the first *satellite* fragmentation and the next *satellite* fragmentation (formation of the purple fragment), and (b) fragments of $n \geq 10^{14}\,{\rm cm}^{-3}$ in the remaining period. Grayscales in figures (a) and (b) denote the density distributions at the stages of Figures 16*c* and 16*e*, respectively.

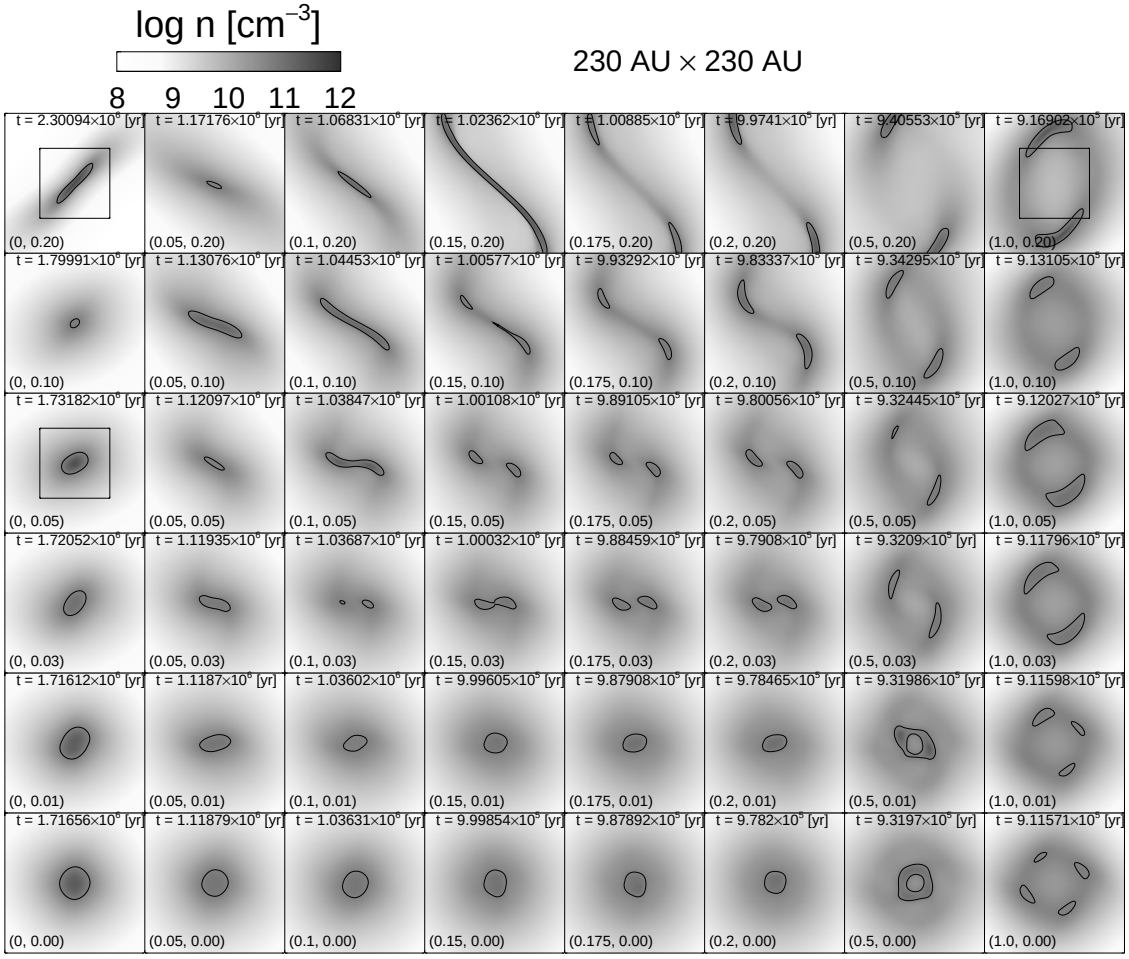

Fig. 19.— Morphology of the central cloud at the stage of $n_{\rm max} \simeq n_{\rm cr}$. Each panel shows the density distribution in the central 230 AU × 230 AU of the $z = 0$ plane. Contour curves denote the critical density $n_{\rm cr}$. Parameters (C, $\Omega_2 t_{\rm ff}$) are noted at the bottom of each panel. Panels are arranged in the order of increasing C from left to right, and increasing $\Omega_2 t_{\rm ff}$ from bottom to top. Initial rotation is $\Omega_0 t_{\rm ff} = 0.2$ for all models.

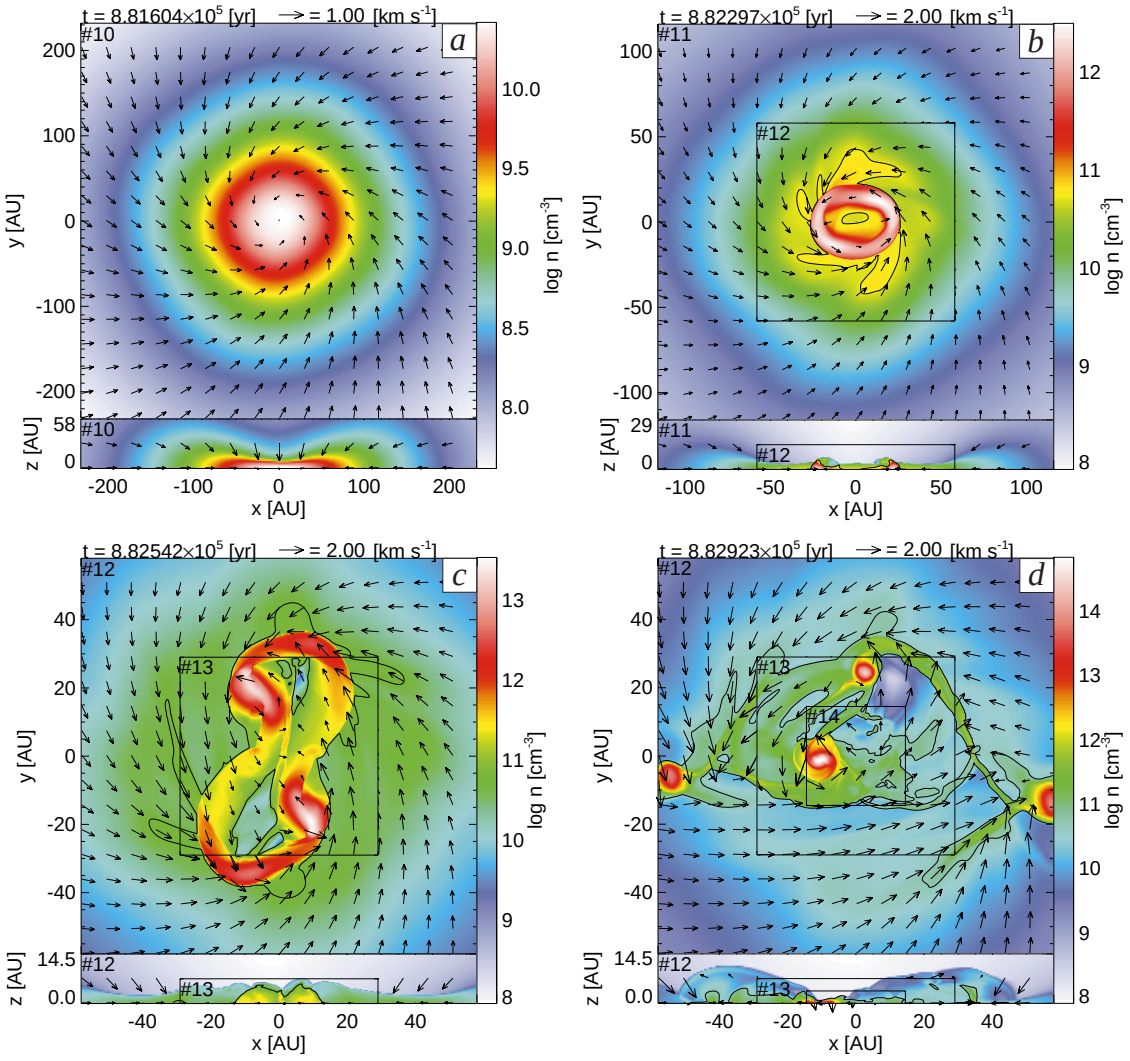

Fig. 20.— Same as Figure 3 but for a model of *ring* type fragmentation, $(\Omega_0 t_{\rm ff}, \Omega_2 t_{\rm ff}, C) = (0.2, 0.0, 1.0)$.

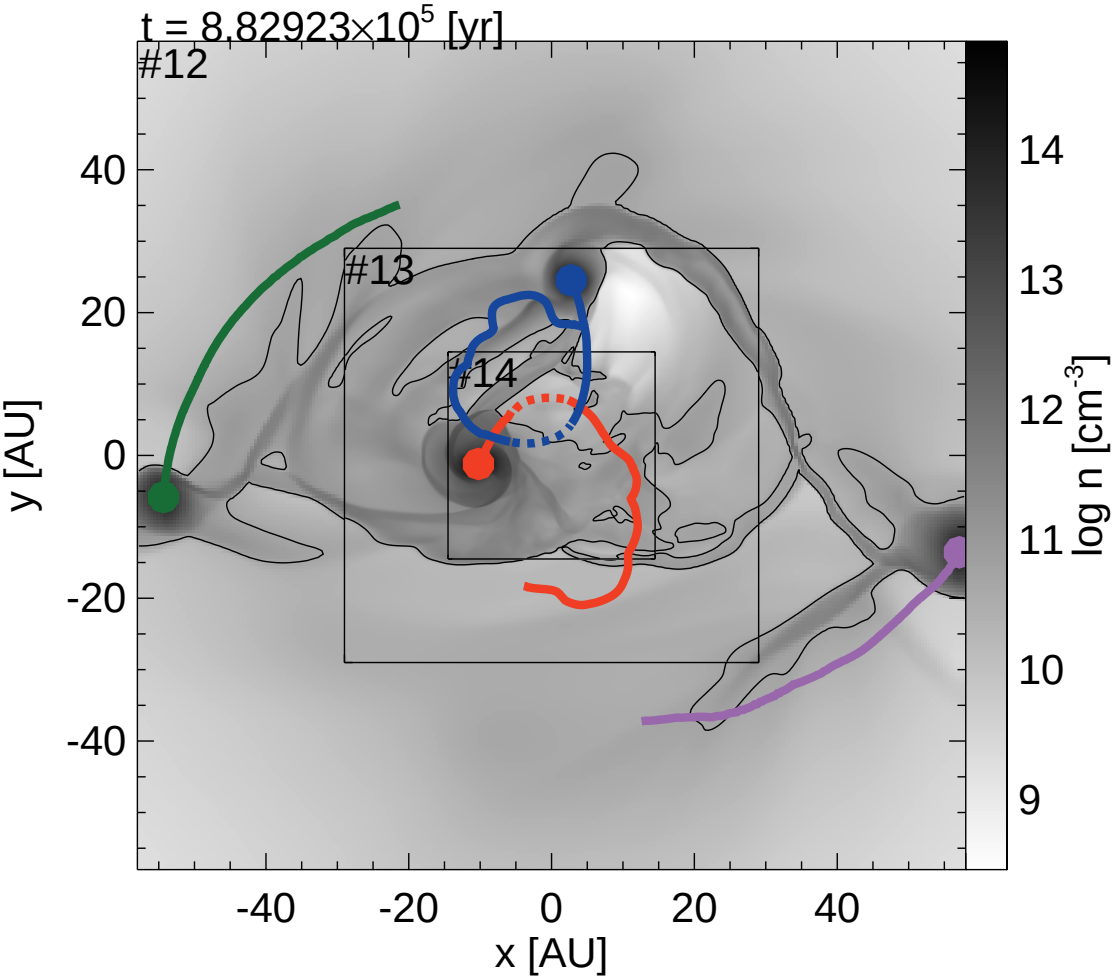

Fig. 21.— Same as Figure 10 but for a model of *ring* type fragmentation, ($\Omega_0 t_{\rm ff}$, $\Omega_2 t_{\rm ff}$, C) = (0.2, 0.0, 1.0). Dashed parts of blue and red loci show schematic orbits, which can not be defined separately because the fragments approach too closely.

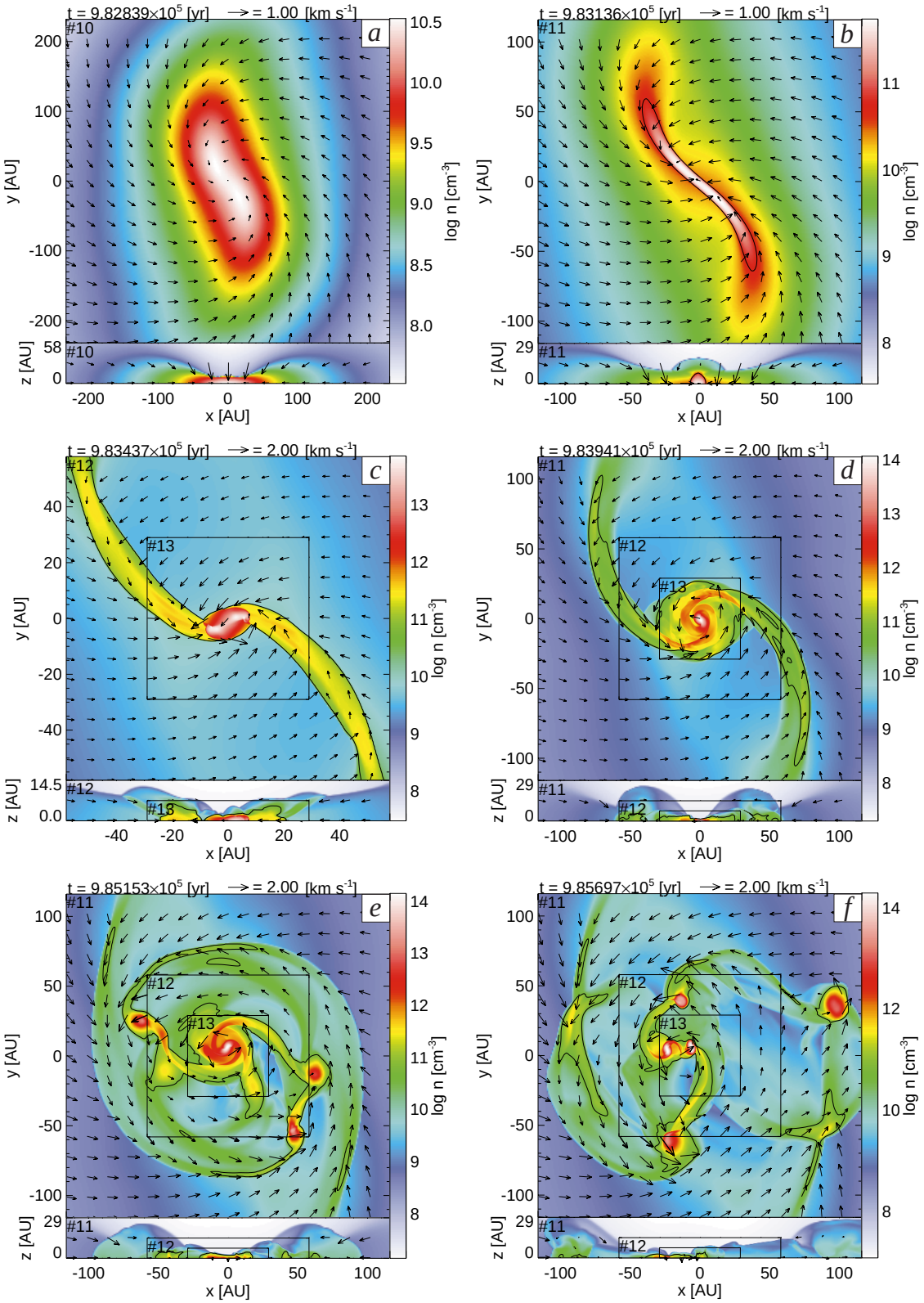

Fig. 22.— Same as Figure 3 but for model a of *bar* type fragmentation followed by *satellite* type fragmentation, $(\Omega_0 t_{\rm ff}, \Omega_2 t_{\rm ff}, C) = (0.2, 0.2, 0.15)$.

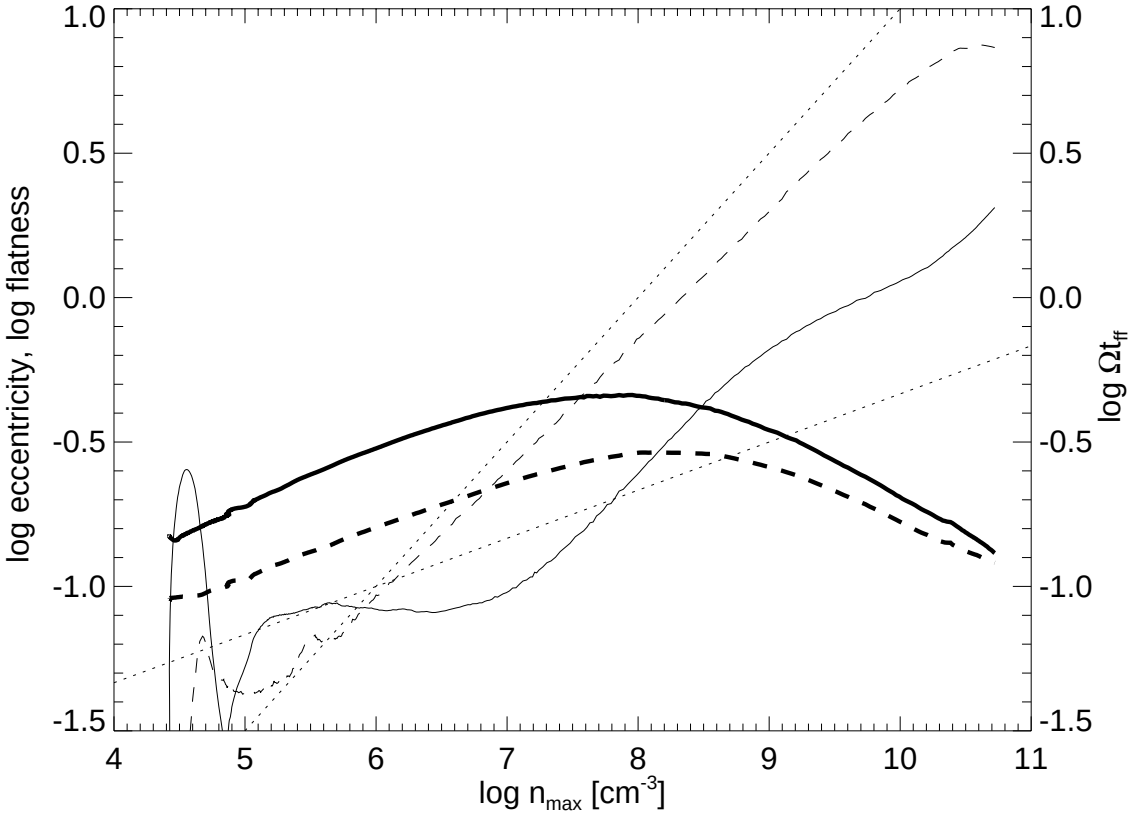

Fig. 23.— Same as Figure 4 but for a model of *bar* type fragmentation followed by *satellite* type fragmentation, $(\Omega_0 t_{\rm ff}, \Omega_2 t_{\rm ff}, C) = (0.2, 0.2, 0.15)$. Dotted curves denote the relationships $\propto n_{\rm max}^{1/6}$ and $n_{\rm max}^{1/2}$ for comparison.

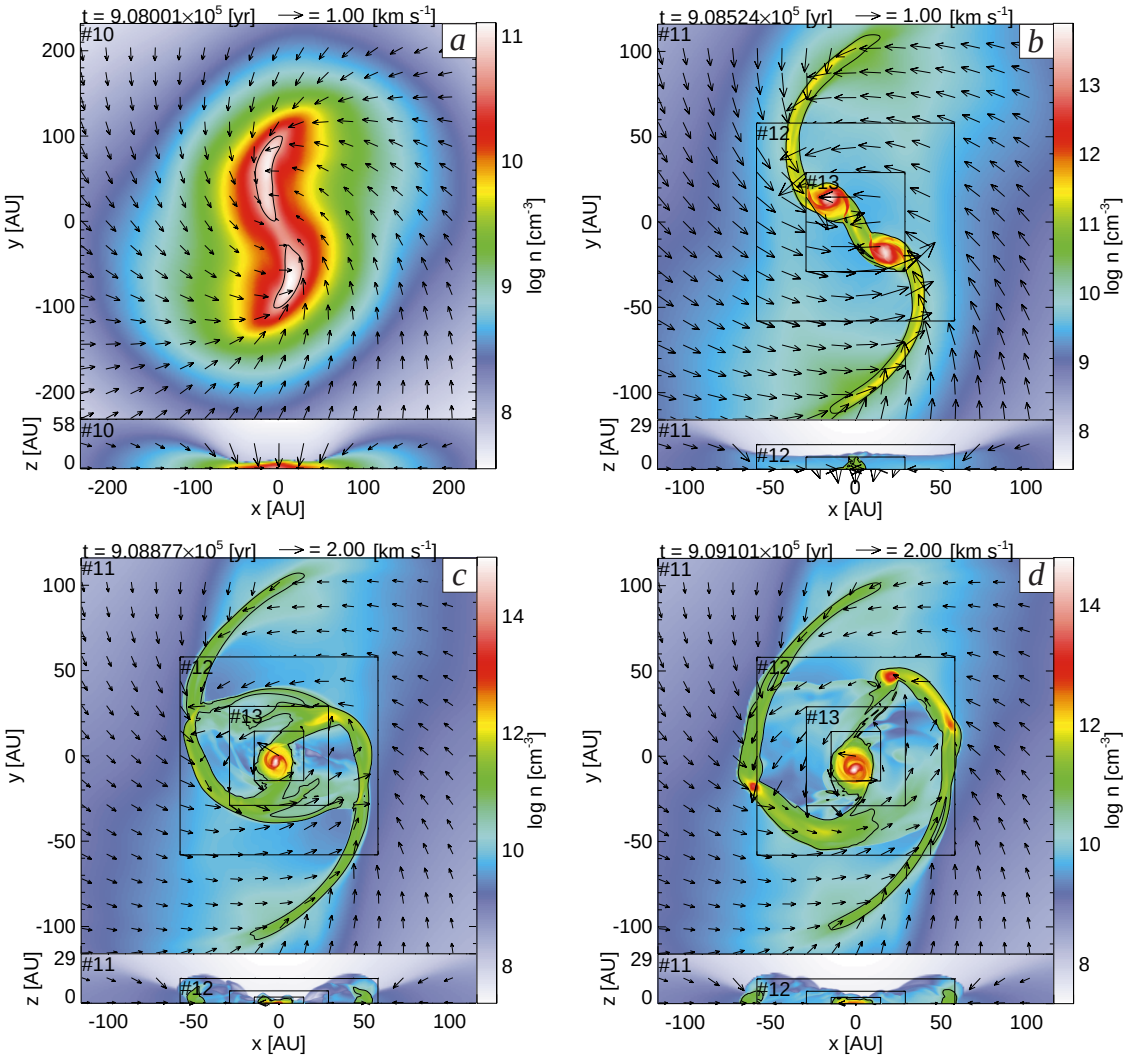

Fig. 24.— Same as Figure 3 but for a model of *dumbbell* type fragmentation followed by *satellite* type fragmentation, $(\Omega_0 t_{\rm ff}, \Omega_2 t_{\rm ff}, C) = (0.2, 0.2, 0.5)$.

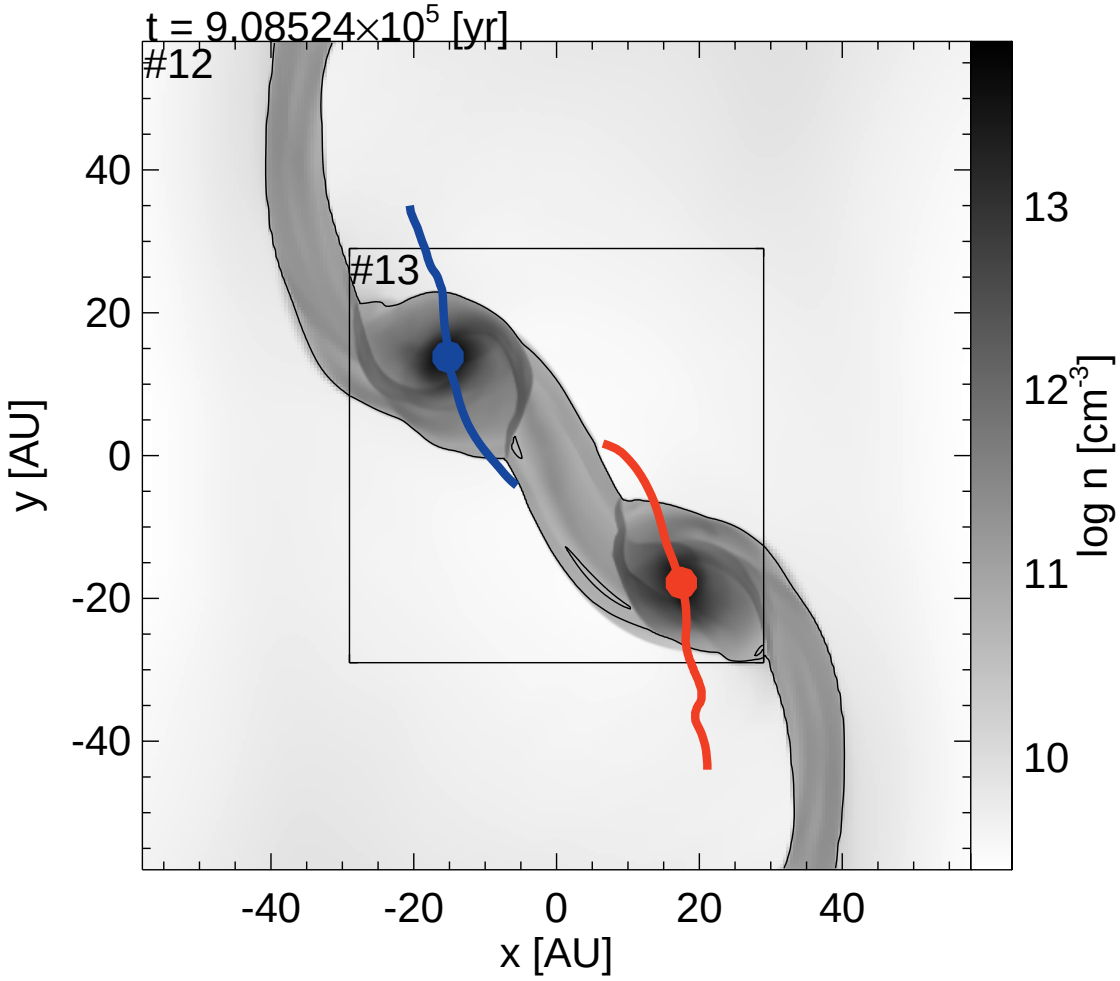

Fig. 25.— Same as Figure 10 but for a model of *dumbbell* type fragmentation followed by *satellite* type fragmentation, $(\Omega_0 t_{\rm ff}, \Omega_2 t_{\rm ff}, C) = (0.2, 0.2, 0.5)$.

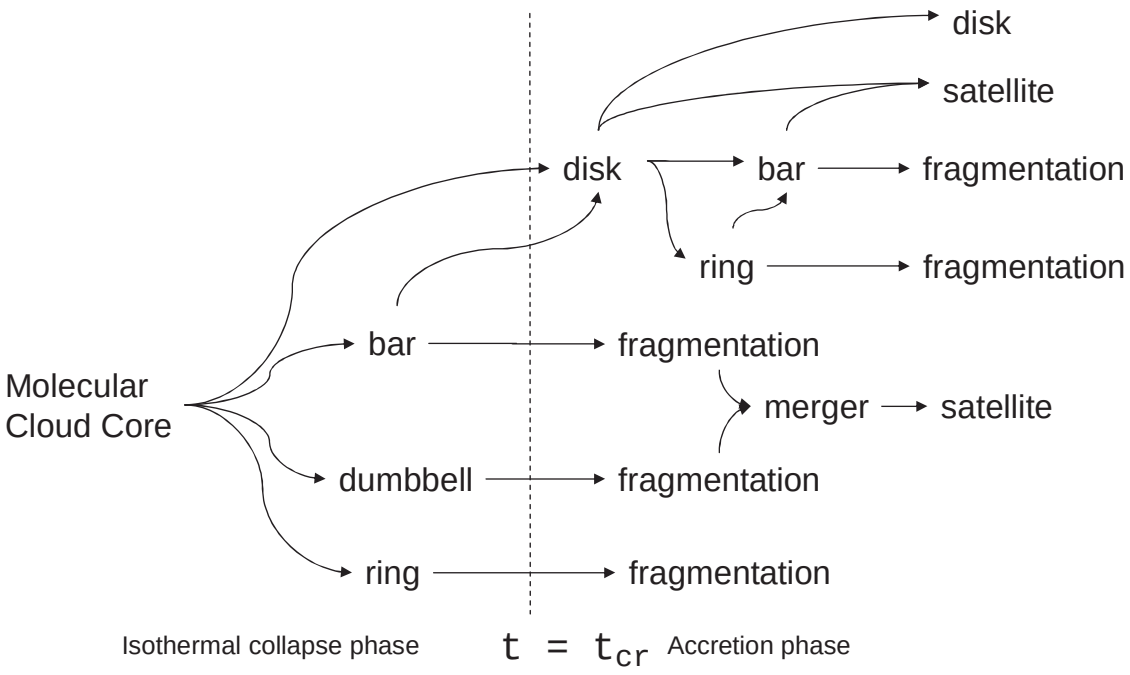

Fig. 26.— Branching of models.

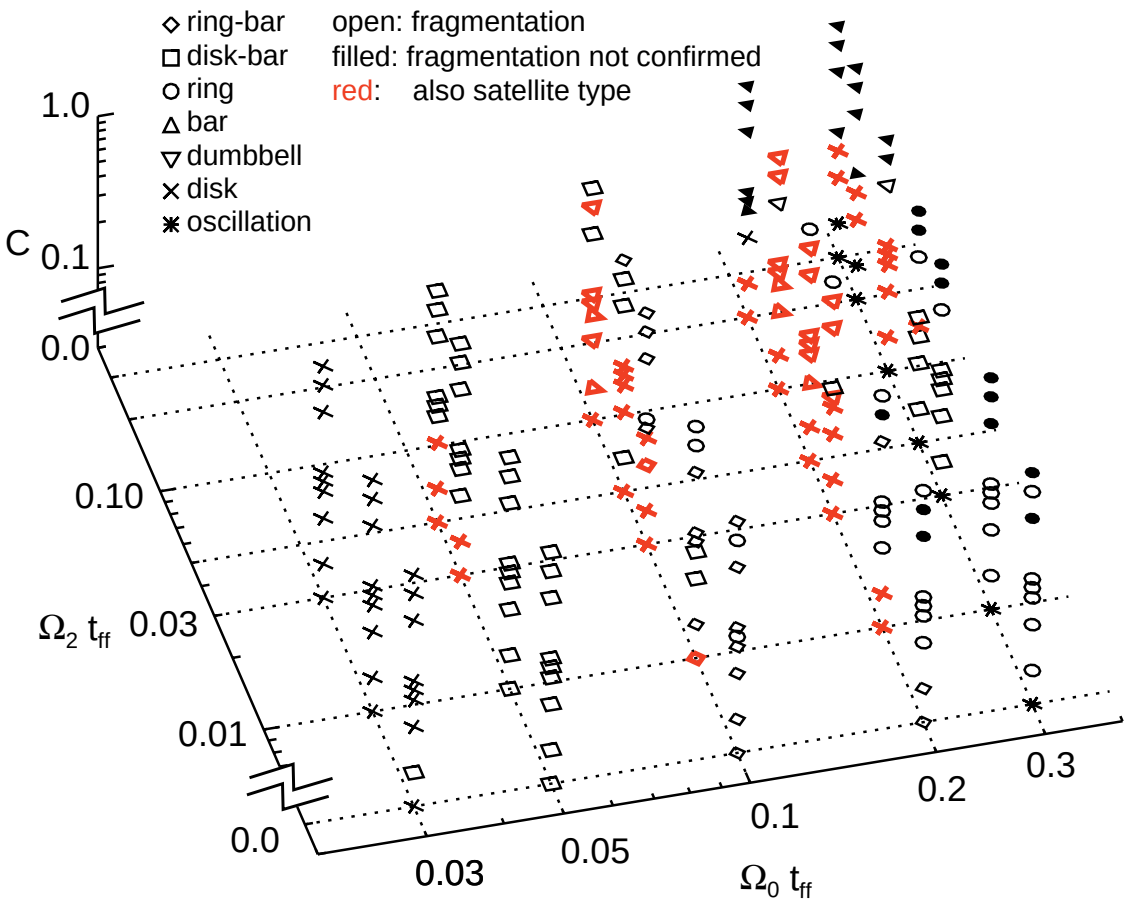

Fig. 27.— Types of collapse and fragmentation in the three-dimensional phase space of ($\Omega_0 t_{\rm ff}$, $\Omega_2 t_{\rm ff}$, C). Red symbols denote the models of *satellite* type fragmentation. For the models indicated by filled symbols, deformation of the central cloud could be followed, but fragmentation could not, or survival of fragments cloud not be confirmed in the simulation.

Table 1. High-resolution models

$\Omega_0 t_{\rm ff}$	$\Omega_2 t_{\rm ff}$	C
0.03	0.03	0.0
0.05	0.0	0.0
0.1	0.0	0.0
0.1	0.03	0.0
0.1	0.1	0.0
0.1	0.05	0.0
0.2	0.2	0.15
0.2	0.2	0.5
0.2	0.2	1.0